Journal of the Meteorological Society of Japan, Vol. 90A, pp. 233–258, 2012.
DOI:10.2151/jmsj.2012-A12

Climate Simulations Using MRI-AGCM3.2 with 20-km Grid

Ryo MIZUTA, Hiromasa YOSHIMURA

Meteorological Research Institute, Tsukuba, Japan

Hiroyuki MURAKAMI, Mio MATSUEDA

Japan Agency for Marine-Earth Science and Technology, Yokohama, Japan

Hirokazu ENDO, Tomoaki OSE, Kenji KAMIGUCHI, Masahiro HOSAKA

Meteorological Research Institute, Tsukuba, Japan

Masato SUGI

Japan Agency for Marine-Earth Science and Technology, Yokohama, Japan

Seiji YUKIMOTO, Shoji KUSUNOKI, and Akio KITOH

Meteorological Research Institute, Tsukuba, Japan

(Manuscript received 21 February 2011, in final form 12 October 2011)

Abstract

A new version of the atmospheric general circulation model of the Meteorological Research Institute (MRI), with a horizontal grid size of about 20 km, has been developed. The previous version of the 20-km model, MRI-AGCM3.1, which was developed from an operational numerical weather-prediction model, provided information on possible climate change induced by global warming, including future changes in tropical cyclones, the East Asian monsoon, extreme events, and blockings. For the new version, MRI-AGCM3.2, we have introduced various new parameterization schemes that improve the model climate. Using the new model, we performed a present-day climate experiment using observed sea surface temperature. The model shows improvements in simulating heavy monthly-mean precipitation around the tropical Western Pacific, the global distribution of tropical cyclones, the seasonal march of East Asian summer monsoon, and blockings in the Pacific. Improvements in the model climatologies were confirmed numerically using skill scores (e.g., Taylor's skill score).

1. Introduction

As progressively more detailed and localized information is required regarding future change in extreme weather and climate events resulting from global warming, there is increasing demand for simulations by high-resolution climate models. Changes are anticipated in the frequency and distribution of disaster events associated with localized heavy rainfall or heavy storms in mountainous regions, such as flooding, landslides, and strong winds. In terms of planning adaptation to such localized changes, even the most recent atmosphere–ocean coupled models do not have sufficient resolution to yield useful information.

By employing atmospheric climate models rather than atmosphere–ocean coupled models, it is

Corresponding author: Ryo Mizuta, Meteorological Research Institute, 1-1 Nagamine, Tsukuba 305-0052, Japan.
E-mail: rmizuta@mri-jma.go.jp

possible to perform long-term climate simulations at a much higher resolution. The use of higher-resolution models (horizontal resolutions up to 20 km) enables the simulation of large-scale phenomena that possess small-scale structures, such as tropical cyclones, and regionally localized phenomena associated with small-scale orography. The statistical climate of such phenomena, such as their geographical frequency distribution, can be obtained by climate simulations performed for periods longer than several decades.

In this context, we developed the Meteorological Research Institute (MRI)/Japan Meteorological Agency (JMA) atmospheric climate model with a 20-km grid (Mizuta et al. 2006). This model is based on the JMA's operational weather prediction model, in which we implemented quasi-conservative semi-Lagrangian dynamics, a radiation scheme, and a land surface scheme developed for a climate model. Simulations of the present-day and future climates were performed by using the observed sea surface temperature (SST) and SST change projected by atmosphere–ocean coupled models as the lower boundary condition. Small-scale phenomena are realistically simulated in the high-resolution model, with keeping the same quality of global-scale climate representation as the lower-resolution models. Accordingly, the future climate simulation results provide a large amount of information including possible changes in tropical cyclones (Oouchi et al. 2006; Murakami et al. 2011), the East Asian monsoon (Kusunoki et al. 2006), extreme events (Kamiguchi et al. 2006), and blocking (Matsueda et al. 2009).

Moreover, various issues related to local and regional climate change were examined using this model. The horizontal resolution employed in the model (20 km) is as fine as that employed by regional climate models (RCMs) in recent studies. Therefore, our model provides information on regions that are covered by few RCMs, including river discharge in a river basin within Colombia (Nakaegawa and Vergara 2010), the Latin America and Caribbean regions (Vergara et al. 2010), and rainfall and temperature in Bangladesh (Rahman et al. 2012). In other regions, our model provides information on regional climate change as well as other RCMs, as shown by Xue et al. (2010) on the model intercomparison of the West African Monsoon, and Jin et al. (2010) on Mediterranean water cycle. In the Japan region, outputs of our model are used as lateral boundary conditions for a non-hydrostatic cloud-resolving RCM with resolutions of 5, 2, and 1 km (Wakazuki et al. 2007). An increase in the 90th percentile values of daily precipitation is projected in the 5-km model, associated with intensified convective instability (Kanada et al. 2010).

However, there were still some biases which were necessary to be improved in the 20-km model, including the geographical distribution of tropical cyclones (Murakami and Sugi 2010) and insufficient precipitation amounts over the Western Pacific. Kang et al. (2002) reported that recent atmospheric general circulation models (AGCMs) still have difficulties in simulating precipitation amounts over the Western Pacific, based on an intercomparison of 10 AGCMs using AMIP-type experiments. A possible solution to this problem is to use a much higher resolution to simulate smaller-scale processes, as shown by the use of a non-hydrostatic AGCM with 7-km grid (Satoh et al. 2008) and by an operational forecast model with 10-km grid (ECMWF 2009). However, not only individual small-scale phenomena but their climatological states and variances are also required to be simulated well at a fine scale to obtain reliable projections related to global warming. To improve the performance of the 20-km model in simulating regional-scale climate, our priority has been placed on refining the physical schemes embedded in the 20-km model.

In the present paper, we introduce new parameterization schemes that yield improvements in the model. Using the new model, we have performed an AMIP-type experiments using observed SST for the present-day climate. The results are compared with those of the same simulation using the previous version of the model (Kitoh et al. 2009).

The remainder of the paper is organized as follows. The improvements made to the model are outlined in Section 2, and the experimental design is presented in Section 3. Section 4 provides an assessment of the model performance in terms of representing the present-day climate of the global seasonal-mean state, variations in the Asian region, and tropical/extratropial storm activity. Finally, summary and discussion are provided in Section 5.

2. Model development

2.1 Model outline

The model used for the experiment is the atmospheric general circulation model of MRI (MRI-AGCM3.2). This is developed as the atmospheric

Table 1. Specifications of the new and previous versions of the model.

	MRI-AGCM3.1S	MRI-AGCM3.2S
Horizontal resolution	TL959 (20 km, 1920 × 960)	TL959 (20 km, 1920 × 960)
Vertical levels	60 (top at 0.1 hPa)	64 (top at 0.01 hPa)
Time step	6 minutes	10 minutes
Cumulus convection	Prognostic Arakawa–Schubert	Yoshimura
Cloud	Smith (1990)	Tiedtke (1993)
Radiation	Shibata and Aoki (1989); Shibata and Uchiyama (1992)	JMA (2007)
Gravity wave drag	Iwasaki et al. (1989)	Iwasaki et al. (1989)
Land surface	Hirai et al. (2007)	Hirai et al. (2007)
Boundary layer	Mellor Yamada (level 2)	Mellor Yamada (level 2)
Aerosol (direct)	Sulfate aerosol	Five species

component of MRI-ESM1 (Yukimoto et al. 2011), which is the earth system model developed by MRI. MRI-AGCM3.2 is based on a model developed jointly by JMA and MRI (Mizuta et al. 2006) and its very slightly revised version (MRI-AGCM3.1) used for the previous 20-km experiments (Kitoh et al. 2009). Many parameterization schemes for various physical processes are newly developed and introduced into the model by both of JMA and MRI. The schemes are implemented to be switched easily from the conventional schemes. The models with 20-km resolution are referred to as MRI-AGCM3.1S and MRI-AGCM3.2S (where 'S' refers to super-high resolution) in the case that we need to distinguish them from lower-resolution models. Table 1 lists the differences between the schemes used for MRI-AGCM3.1S (hereafter v3.1) and for the new MRI-AGCM3.2S (hereafter v3.2). This section provides an overview of the differences between the models.

2.2 *Dynamical framework*

The dynamical framework remains unchanged from the previous model, which is a hydrostatic primitive equation system using a spectral transform method of spherical harmonics, as originally designed by Kanamitsu et al. (1983). A two-time-level semi-implicit semi-Lagrangian scheme is used for time integration (Yoshimura and Matsumura 2005). Improvements in the computational stability of the semi-Lagrangian scheme are implemented in the new model, enabling an increase in the time step from 6 to 10 minutes.

The highest-resolution experiments are performed at a triangular truncation at wave number 959 (TL959) in the horizontal, for which the transform grid uses 1920 × 960 grid cells, corresponding to a grid interval of roughly 20 km. The number of vertical levels has been changed from 60 layers (top at 0.1 hPa) in the previous model to 64 layers (top at 0.01 hPa) in the new model. Only those levels above the tropopause have been changed.

2.3 *Cumulus convection*

A new cumulus parameterization scheme, based on a scheme by Tiedtke (1989), has been developed and introduced to the model, replacing the prognostic Arakawa–Schubert scheme (Arakawa and Schubert 1974; Randall and Pan 1993). The description of the new scheme, called the Yoshimura cumulus scheme, is summarized by Yukimoto et al. (2011). Arakawa–Schubert-type schemes and Tiedtke-type schemes are both categorized as mass-flux type cumulus schemes. In the Arakawa–Schubert-type scheme, multiple convective updrafts with different heights (depending on the entrainment rate) are explicitly calculated within a single grid cell (Fig. 1a), although each updraft is a simplified entraining plume. In the Tiedtke-type scheme, on the other hand, only a single convective updraft is calculated within a single grid cell, but is represented as a more detailed entraining and detraining plume (Fig. 1b). In the new scheme, detailed entraining and detraining plumes (as with the Tiedtke-type scheme) are calculated for two convective updrafts within a single grid cell. The two updrafts represent the tallest updraft with a minimum turbulent entrainment rate, and the shortest updraft with a maximum turbulent entrainment rate. Multiple convective updrafts with different heights (as with the Arakawa–Schubert-type scheme) are assumed to exist, where temperature, the water vapor mixing ratio, the entrainment rate, and other variables are obtained by linear interpolation between the two extreme updrafts (Fig. 1c).

During the development phase of the cumulus

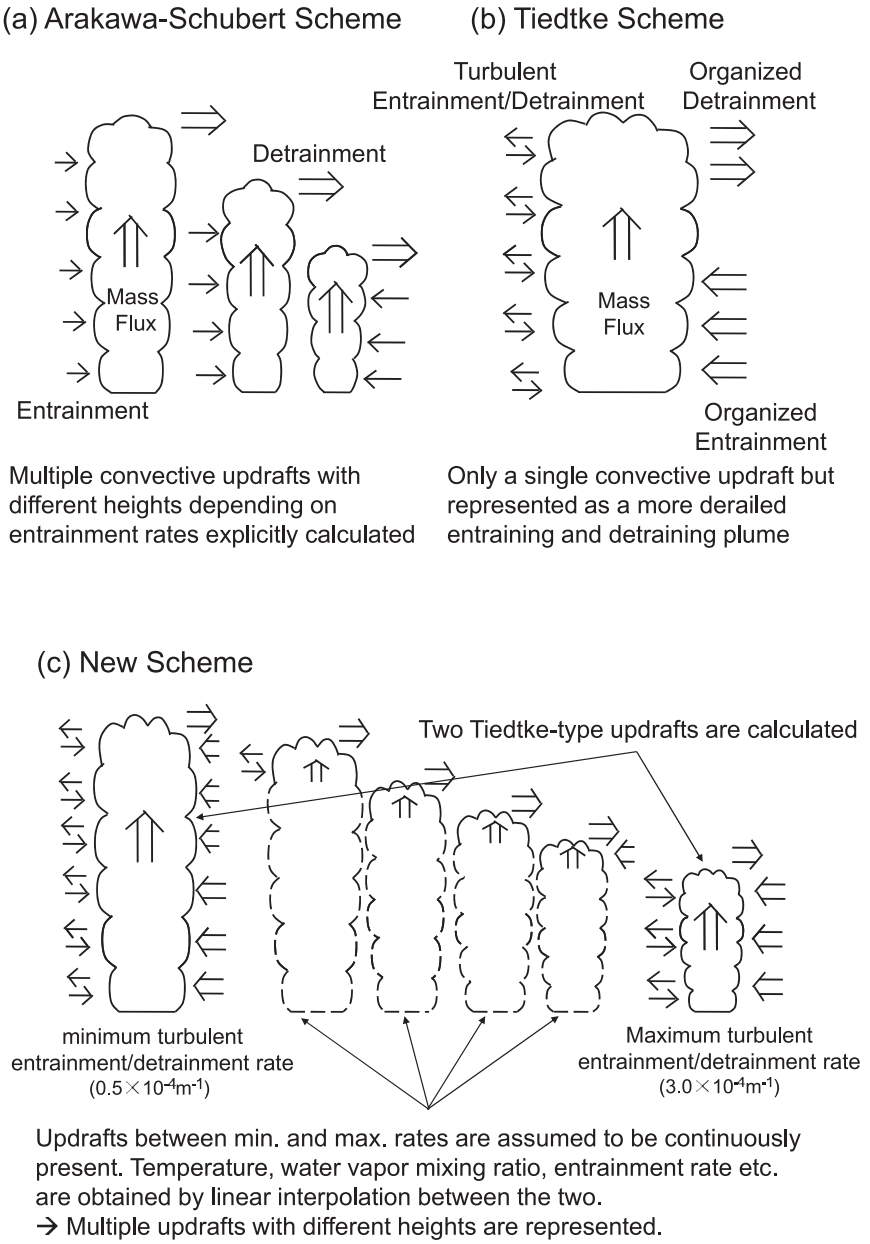

Fig. 1. Schematic diagrams of (a) Arakawa–Schubert-type, (b) Tiedtke-type, and (c) the introduced cumulus schemes.

parameterization scheme, modifications are made in terms of how the model can capture the characteristics of the real atmosphere. In the new scheme, there are arbitrary assumptions in determining the organized entrainment, similarly to the Tiedtke scheme. Precipitation in the areas upstream of mountains (e.g., the northeastern part of the Bay of Bengal) has been enhanced by assuming that the organized entrainment is approximately proportional to the horizontal convergence at each grid-point. Under this assumption, the organized entrainment becomes smaller in the areas upstream of mountains, which is thought to promote the development of cumulus convection. In addition, the organized entrainment above the level of minimum moist static energy has also been taken into ac-

count. That has affected mean precipitation and tropical cyclone genesis over the tropics.

Moreover, two further modifications has been implemented in the conversion of cloud water to precipitation within the updraft. One is reducing the conversion rate. By reducing the conversion rate, the detrained cloud amount has been increased, affecting the reflection of shortwave radiation and the mean precipitation over the tropics. The other is suppressing the conversion near the cloud bottom. The conversion from cloud water to precipitation is suppressed between the cloud bottom and a specified distance from the cloud bottom. An increase in this distance results in the enhanced detrainment of cloud water, especially just above the boundary layer, which facilitates the organization of convection around the lower troposphere.

2.4 *Cloud*

The previous version of the model used a large-scale cloud scheme similar to that proposed by Smith (1990), in which cloud water and cloud amount are estimated by a simple statistical approach. In the new version of the model, the Tiedtke cloud scheme (Tiedtke 1993; ECMWF 2004; Jakob 2001) is incorporated and used (Kawai 2006). Cloud water and cloud amount are treated as prognostic variables in the scheme. Clouds are formed via adiabatic and diabatic cooling, and via detrainment from the cumulus convection scheme. The model considers the dissipation of clouds through evaporation by heating, evaporation by turbulent mixing with a surrounding air mass, and conversion to precipitation. The new model does not use a parameterization specific to stratocumulus, while a simple parameterization of stratocumulus was used in the previous model.

2.5 *Radiation*

The radiation scheme has been changed to the same scheme used in the JMA operational model (JMA 2007), except for the interaction with aerosols. Infrared (longwave) radiation (up to 3000 cm^{-1}) and solar (shortwave) radiation are treated separately. Because of the relatively large computational cost, full radiation computations are made for every two grid-spacings in the zonal direction, and for every 1 and 3 hours in the shortwave and longwave regions, respectively. The calculated values are adjusted for each grid of each time step depending on its own solar zenith angle and surface temperature. The spectrum is divided in 9 bands in the longwave region and 22 bands in the shortwave region, and the radiative flux is calculated in each band. The model considers major absorptions due to water vapor (line and continuum absorption), carbon dioxide (in the 15 μm band, near-infrared region, etc.), and ozone (in the 9.6 μm band, visible and ultraviolet region). Also taken into account is absorption due to methane (CH_4), dinitrogen monoxide (N_2O), and chlorofluorocarbons (CFCs) in the longwave scheme, for consideration of their greenhouse effect. Absorption by oxygen and Rayleigh scattering by molecules of atmospheric gas is also calculated in the shortwave radiation.

2.6 *Aerosol*

In the representation of the direct effect of aerosol, optical parameters are configured to five types of aerosol species: sulfate, black carbon, organic carbon, mineral dust, and sea-salt. The extinction/absorption coefficients and asymmetry factors for these species are computed based on an assumption of Mie scattering by spherically shaped particles, based in turn on complex refraction index data from OPAC (Optical Properties of Aerosols and Clouds) by Hess et al. (1998). For species with hygroscopic properties, the model considers their dependency on ambient relative humidity (Chin et al. 2002). The indirect effects of aerosol are not considered in this experiment. The effective radius of ice cloud particles is parameterized depending only on cloud water content, based on McFarquhar et al. (2003).

2.7 *Other schemes*

The level 2 turbulence closure scheme by Mellor and Yamada (1974) is used as the planetary boundary layer scheme in v3.2, as with v3.1. The land-surface scheme by Hirai et al. (2007), improved from the Simple Biosphere model, is also used in v3.2, as with v3.1.

To represent diurnal temperature variations at the air–sea interface due to short-term variations in wind and solar radiation, a simple skin sea-surface scheme is introduced. As described by Yukimoto et al. (2011), the scheme has one sub-skin layer with a thickness of 1 m. The coefficient for the heat flux from the bottom of the layer depends on the wind speed. Temperature at the bottom of the layer (1 m below the air–sea interface) is given from the boundary condition file, and the temperature at the air–sea interface is calculated and used as the lower boundary of the atmospheric model. Using this scheme, the interface temperature in

the model shows diurnal variations of up to 2 K on moderately clear days in the tropics, which is comparable to observed values (Yasunaga et al. 2008). For most regions, the difference between the monthly mean of the calculated skin temperature and the given SST is less than 0.1 K.

The model uses the orographic gravity wave drag scheme by Iwasaki et al. (1989), in which gravity waves are partitioned into long waves (wavelength $\geq$ 100 km) and short waves (wavelength $\sim$ 10 km). The long waves propagate upward and deposit momentum in the middle atmosphere, while the short waves are trapped in the troposphere and exert drag in this region. The drag coefficients in v3.2 are the same as those in the operational model (JMA 2007), which are smaller than the values in v3.1. A Rayleigh friction term is introduced above 50 hPa.

3. Methods

3.1 Experimental settings

The ability of the new model (v3.2) to simulate the climate is examined by performing an AMIP-type experiment for the period from 1979 to 2003. Monthly-mean data from HadISST1 (Rayner et al. 2003) with $1^\circ \times 1^\circ$ resolution for 1979–2003 are used for the observed SST and sea-ice concentration data, along with the monthly climatology of sea ice thickness from Bourke and Garrett (1987). Concentrations of greenhouse gases (CO_2, CH_4, N_2O, and CFCs) are set to the observed global-mean, annual-mean values, changing from year to year. Three-dimensional, monthly-mean distributions of ozone and aerosols are also given as boundary conditions. The ozone is from the results of the Reference Simulation 2 for the Chemistry Climate Models Validation (Eyring et al. 2005) using the MRI Chemical Transport Model (Shibata et al. 2005). The aerosols are from the results of a present-day experiment using a prototype version of MRI-ESM1, in which the historical emission flux of anthropogenic SO_2, invariant SO_2 flux from non-eruptive volcanoes, and the surface emission inventories for carbonaceous aerosols are prescribed (Yukimoto et al. 2011). The 5-year running means of both results are incorporated into the model. We do not use the observed ozone and aerosol distributions because this experiment is carried out as the 'control' climate simulation to be compared against the global warming simulation forced by warmed surface conditions, increased concentrations of greenhouse gas, and changed ozone/aerosol distributions.

The results are compared with the same AMIP-type experiment performed using v3.1 (Kitoh et al. 2009). The same SST, sea-ice concentration, and sea-ice thickness were used, but the zonal-mean ozone is used instead of three-dimensional ozone, and aerosols from a previous version of the MRI aerosol chemical transport model (Tanaka et al. 2003) were used in the v3.1 experiment.

3.2 Observational and reanalysis climatologies

The results of the experiments are evaluated by comparison with observational and reanalysis climatologies. The Japanese 25-year Re-Analysis (JRA-25; Onogi et al. 2007), with a spatial resolution of 1.25° longitude by 1.25° latitude, is used as the reanalysis climatology. ERA40 (Uppala et al. 2005) is used as an additional reanalysis climatology. The climatology of radiation at the top of the atmosphere is compared with satellite measurements from ERBE (Harrison et al. 1990). We use precipitation datasets from CMAP (Xie and Arkin 1997), GPCP (Huffman et al. 2001; Adler et al. 2003), and TRMM-3B43 (Huffman et al. 2007), which are based on sensors onboard satellites and rain gauge observations. In addition, we also use precipitation data with relatively high resolution; that is, APHRODITE daily grid precipitation (Yatagai et al. 2009) based only on rain gauge observation data, and TRMM-3A25 (Iguchi et al. 2000) based only on radar observations from onboard satellite measurements.

4. Results

4.1 Global climate

a. Precipitation

Figure 2 shows the horizontal distributions of long-term mean precipitation for v3.2, the difference between v3.2 and CMAP, and the difference between v3.1 and CMAP, from December to February (DJF) and from June to August (JJA). Although v3.1 performs well in capturing the seasonal-mean spatial patterns (e.g., ITCZ, SPCZ, Asian summer monsoon, and wintertime storm tracks; Mizuta et al. 2006), the degree of bias from observations is reduced in v3.2. In DJF, overestimations are reduced around the eastern Pacific, western Atlantic, and western Indian Ocean near the equator. In JJA, v3.2 shows an improvement in regions of heavy rainfall from the South China Sea to the tropical Western Pacific, for which an underestimate was obtained from v3.1. This improvement is due mainly to refinements in the perfor-

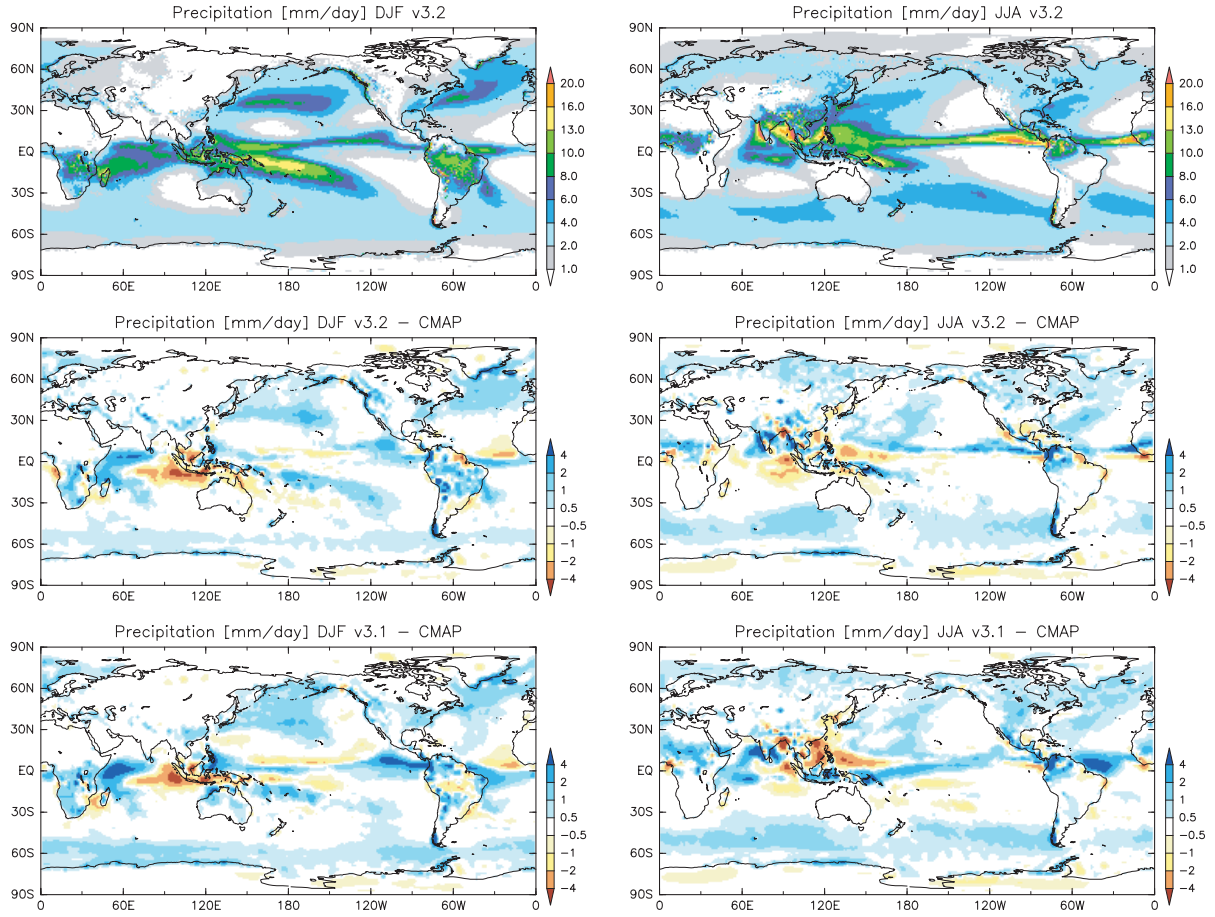

Fig. 2. Horizontal distribution of long-term mean precipitation (mm day^{-1}) in (left) December to February (DJF) and (right) June to August (JJA) for (top) v3.2, (middle) difference between v3.2 and CMAP, and (bottom) difference between v3.1 and CMAP.

mance of the new cumulus scheme, as described in Section 2. In the Arakawa–Schubert scheme used in v3.1, it is difficult to simulate the precipitation pattern around the Western Pacific without unrealistic parameter settings. Some improvements are also seen around India, as described in Section 4.2, although overestimates remain. Overestimates also remain in the eastern part of the ITCZ and in the tropical eastern Atlantic. In the extratropics, there is little difference between v3.1 and v3.2. Biases in the extratropics of the Southern Hemisphere are slightly improved in both seasons. The global annual average precipitation rate is reduced from 3.09 mm day^{-1} (v3.1) to 3.01 mm day^{-1} (v3.2), which remains higher than those in CMAP (2.67 mm day^{-1}) and GPCP (2.61 mm day^{-1}).

Zonal-mean precipitation in DJF and JJA is shown in Fig. 3. In v3.2, seasonal fluctuations in the tropical precipitation peak are clearer than in v3.1; that is, the overestimations around 0–10°N in DJF and 0–10°S in JJA, found in v3.1, are reduced in v3.2. Precipitation around 10°N–20°N in JJA remains more than that observed, corresponding to the overestimation around India, the eastern part of the ITCZ, and the tropical eastern Atlantic (Fig. 2). Zonal means in the extratropics agree well with the estimation of GPCP in both seasons, while an overall overestimation is seen when compared with CMAP.

b. Surface temperature

Figure 4 shows the horizontal distributions of climatological monthly-mean surface temperature in January and July for v3.2 and v3.1, with the differences from the climatology of JRA25 reanalysis. The surface air temperature in the model is defined

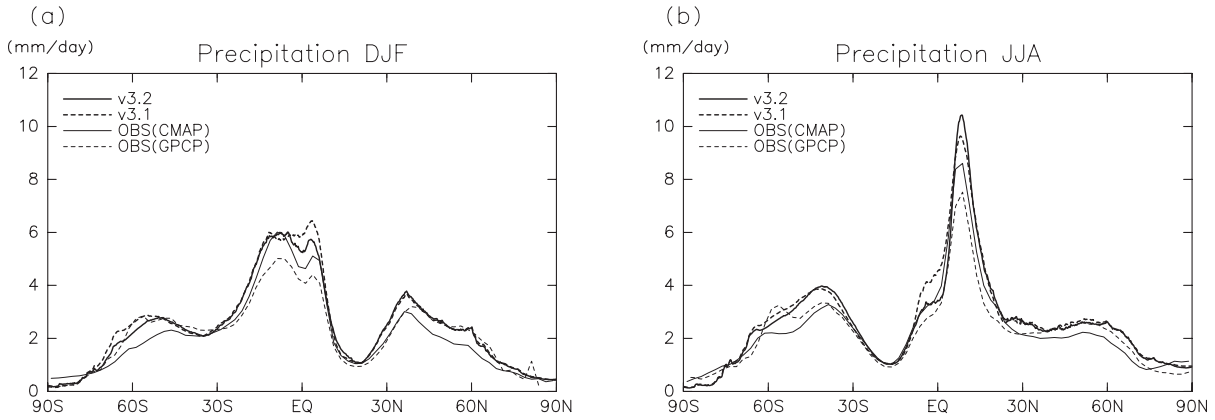

Fig. 3. Zonal-mean precipitation (mm day^{-1}) in (a) DJF and (b) JJA for v3.2 (thick solid line), v3.1 (thick dashed line), and the climatological estimates of CMAP (thin solid line) and GPCP (thin dashed line).

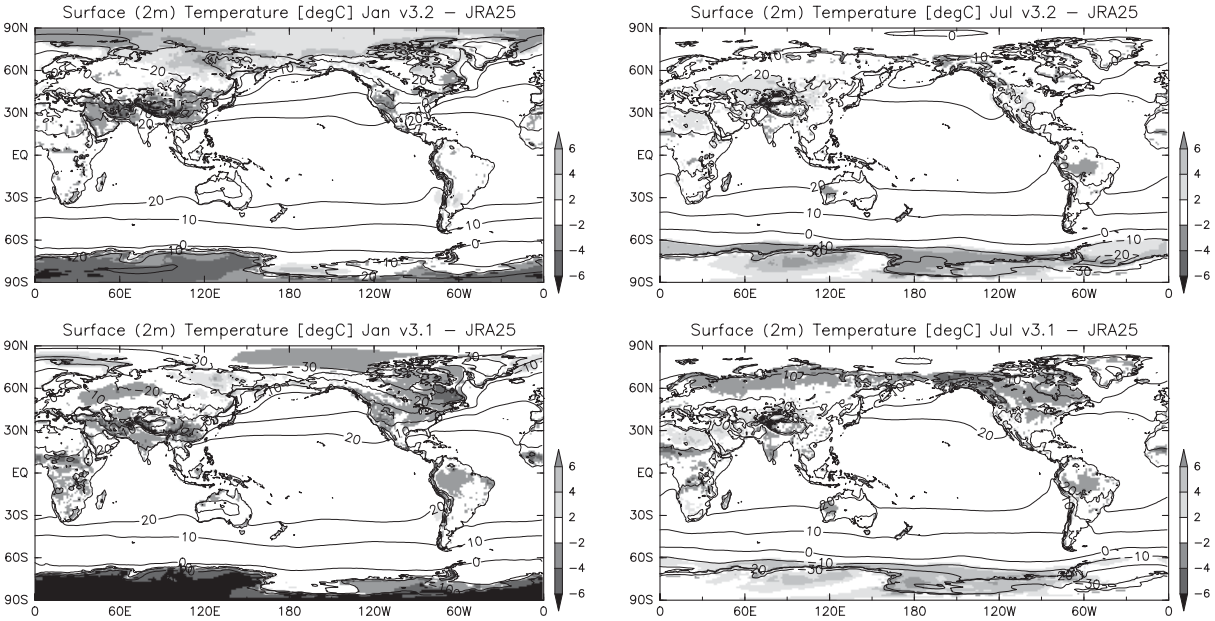

Fig. 4. Horizontal distribution of climatological monthly-mean surface (2 m) temperature (°C) in (left) January and (right) July for (top) v3.2, (bottom) v3.1. Shading indicates differences from the climatology of JRA25 reanalysis.

as air temperature 2 m above the surface, which is diagnosed from the vertical temperature profile of the lowest model layers. Underestimation of the temperature is reduced in v3.2 around North America and the central Africa in both season. A reduction of bias is also seen around the Amazon in January and the northern part of Russia in July, while an enhancement of bias is seen around the northern part of China.

c. Zonal wind and temperature

Figure 5 shows seasonal averages of zonal-mean temperatures and zonal wind velocities for v3.2 and v3.1, along with the difference from the climatology of JRA25 reanalysis. In v3.1, the difference in zonal-mean temperature (Fig. 5b, d) is already within 2 K in most regions of the troposphere, except for the tropical upper troposphere. The bias in the tropical upper troposphere is greatly reduced in

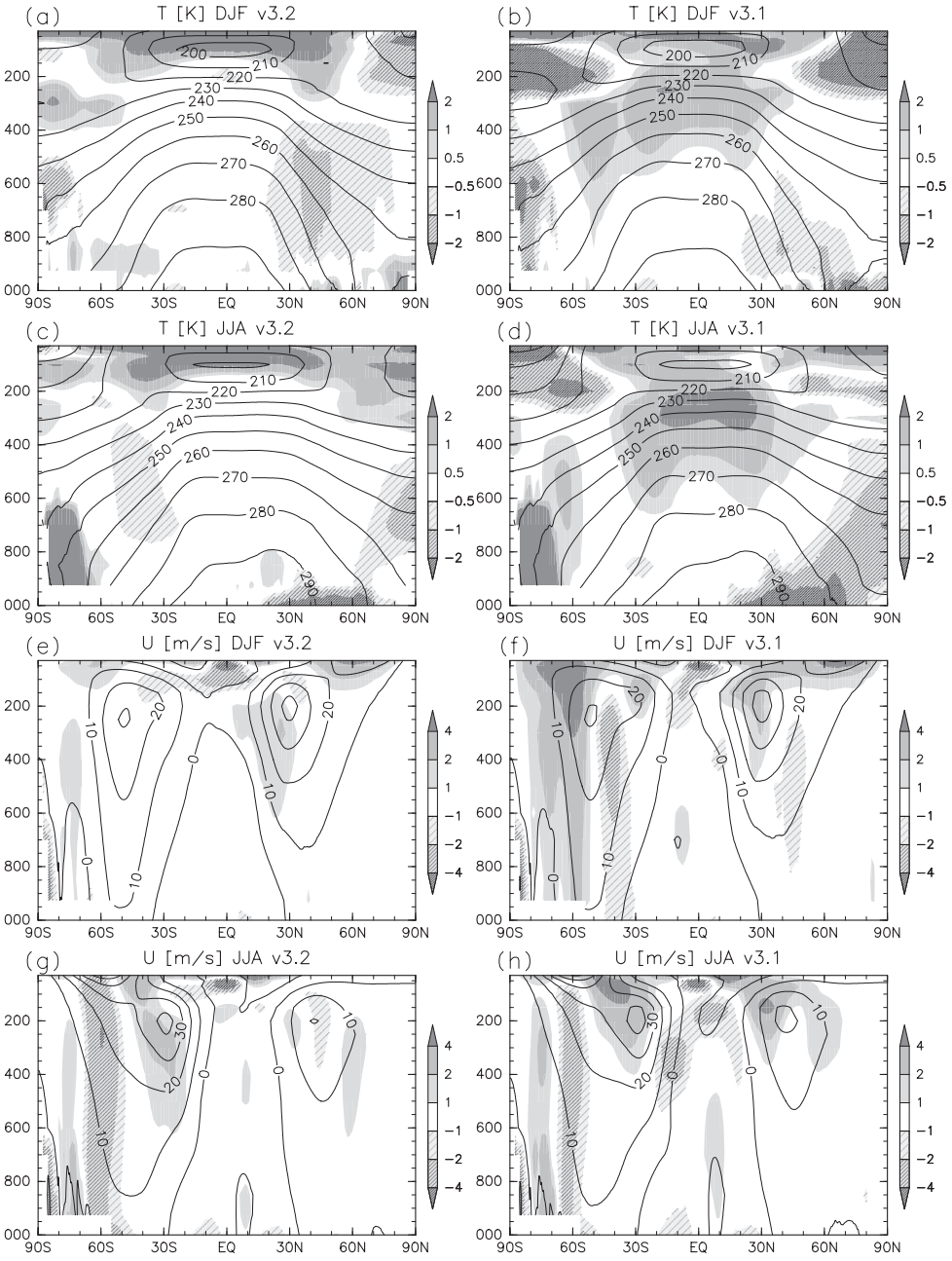

Fig. 5. Seasonal averages of (a–d) zonal-mean temperatures and (e–h) zonal wind velocities in (a, b, e, f) DJF and (c, d, g, h) JJA, for (a, c, e, g) v3.2 and (b, d, f, h) v3.1. Shading indicates differences from the climatology of JRA25 reanalysis. Units are K in (a–d) and m s^{-1} in (e–h).

v3.2 (Fig. 5a, c), and the difference from the reanalysis is within 1 K in the troposphere, except for the wintertime mid-latitudes of the Northern Hemisphere, which has large interannual variability. However, the temperature is higher than the reanalysis and v3.1 in the tropical stratosphere, mainly because the given ozone distribution, which is derived from present-day experiments using a chemical transport model, yield a bias from observed data.

Zonal-mean zonal wind also becomes closer to the reanalysis in v3.2 (Fig. 5e, g) compared with v3.1 (Fig. 5f, h), especially in the extratropics of the Southern Hemisphere in DJF. In addition, around the subtropical jet at 100–200 hPa, overestimations of about 3 m s^{-1} are seen in both hemispheres of both seasons in v3.1 and are reduced in v3.2. They are consistent with an improvement in the meridional temperature gradient between the tropical upper troposphere and extratropics.

d. Z500

Seasonal averages of 500 hPa height during DJF and JJA for each hemisphere are shown in Fig. 6. Shading indicates differences from the climatology of JRA25 reanalysis. In the Northern Hemisphere in DJF (Fig. 6a, e), a common pattern of the bias is seen in v3.1 and v3.2, that is, positive bias around the northern part of Russia and eastern North Pacific, and negative bias around central Asia and the east of Japan. The amplitude of the bias pattern is much smaller in v3.2, while negative bias is seen around North America. The seasonal average becomes closer to the reanalysis climatology also in the Southern Hemisphere in DJF (Fig. 6b, f), where there was a zonal structure of positive (near 45°S) and negative (near the South Pole) biases in v3.1. In the Northern Hemisphere in JJA (Fig. 6c, g), overestimation around North Pacific and underestimation around North America are reduced in v3.2. The improvements in this region in the both season could be related to the improvements in the tropical convective activity through teleconnection patterns. However, relatively large bias remains in the Southern Hemisphere in JJA (Fig. 6d, h).

e. Skill scores

The degree to which the monthly climate of the model averaged over 25 years is different from the observations and the reanalysis is evaluated using a skill score defined by Taylor (2001). We also assess the change in skill score from v3.1 to v3.2. The monthly-mean spatial patterns of various variables are compared with those of an observationally based climatology, using the ratio of the model's standard deviation to that from observations ($\hat{\sigma}_f$) and the correlation coefficients (R).

Figure 7 shows Taylor's diagrams for the global and tropical regions for the monthly climate in January and July averaged over 25 years, for precipitation, wind/height fields, and radiation at the top of

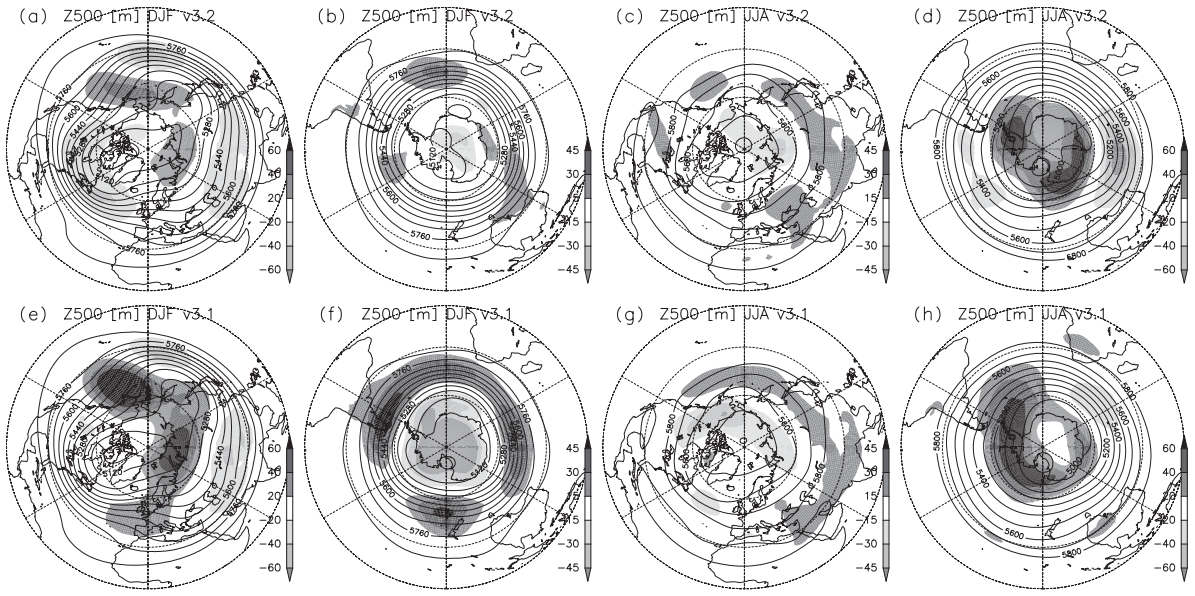

Fig. 6. Seasonal averages of 500 hPa height (m) in (a, b, e, f) DJF and (c, d, g, h) JJA, for (a–d) v3.2 and (e–h) v3.1. (a, c, e, g) are for the Northern Hemisphere, and (b, d, f, h) are for the Southern Hemisphere. Shading indicates differences from the climatology of JRA25 reanalysis. Different shading intervals are used between winter hemisphere and summer hemisphere, according to the different amplitudes of interannual variation.

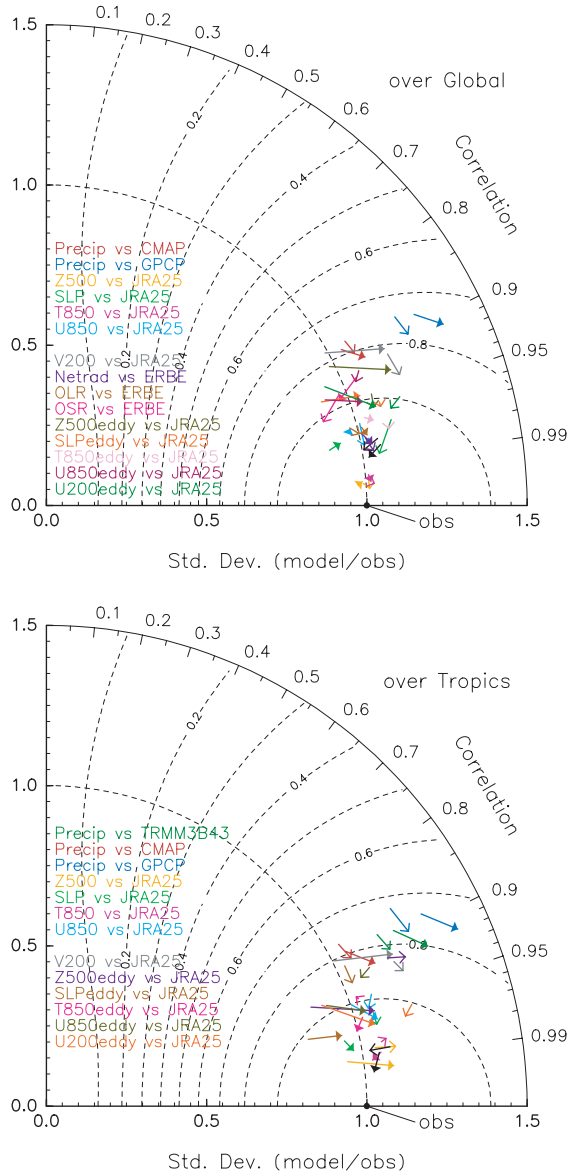

Fig. 7. Taylor diagrams for (top) the global and (bottom) the tropics (60°E–150°E, 0°–30°N). The statistics for v3.1 are plotted at the tail of the arrows, and the arrowheads point to the statistics for v3.2. Arrows with open arrowheads indicate the statistics for January, and those with closed arrowheads indicate the statistics for July. The isolines denote the Taylor skill score. The terms "Precip", "Z", "SLP", "T", "U", and "V" indicate precipitation, geopotential height, sea level pressure, temperature, zonal velocity, and meridional velocity, respectively. The terms "Netrad", "OLR", and "OSR" denote the net, longwave, and shortwave radiation at the top of the atmosphere, respectively.

the atmosphere. The distance from the origin is $\hat{\sigma}_f$, and R is the cosine of the polar angle. Arrows indicate the evolution of the fields from v3.1 to v3.2. The isolines denote the skill score, which is defined as

$$S = \frac{4}{(\hat{\sigma}_f + 1/\hat{\sigma}_f)^2} \frac{(1+R)^4}{(1+R_0)^4}. \quad (1)$$

Here, R_0 is the maximum correlation attainable and set to 1. The distribution of precipitation is compared with two or three observational datasets (CMAP, GPCP, and TRMM in the tropics). Some variables are also evaluated by eddy (deviation from the zonal-mean). The obtained score values are listed in Table 2.

For the global patterns, most of the variables have better scores in v3.2 than in v3.1. Precipitation patterns show an improvement when using GPCP as the reference, as well as when using CMAP as the reference. While the standard deviations become larger and depart from the observations for some variables, the correlation coefficients become higher, resulting in higher skill scores. For January, all the variables for the global domain listed here show improvements from v3.1 to v3.2. The patterns over the tropics are also improved, except for some variables (e.g., geopotential height at 500 hPa and temperature at 850 hPa).

We also performed 25-year simulations with lower spatial resolutions of TL319 (60 km) and TL95 (180 km), using the same model without changing the parameter settings in the physical schemes. The vertical levels are the same (64 levels), and the time steps are 20 minutes for TL319 and 30 minutes for TL95. At each resolution, an improvement in skill score is seen compared with v3.1 in many of the variables (data not shown). Among the three resolutions of v3.2, the score is better in the higher-resolution model than in the lower-resolution model, showing the advantage of enhanced resolution due to better representation of topographical effects and physical processes. However, the resolution dependence of the results in the global-scale climate is small in v3.2, whereas the global-mean precipitation amount was resolution-dependent in the previous version of the model (Mizuta et al. 2006).

4.2 Asian monsoon

a. Asian summer monsoon

Figure 8 shows the simulated JJA-mean precipitation and vertically integrated moisture flux clima-

Table 2. Skill scores (see Taylor 2001) for the global and tropical (25°S–25°N) distribution of monthly means over the 25-year simulation for different variables, and different observational and reanalysis datasets. Bold entries indicate that the score is better than that obtained for the other model.

			January		July	
Variable	Obs. Dataset	Region	v3.1	v3.2	v3.1	v3.2
Precip	CMAP	Global	0.7716	**0.8030**	0.7862	**0.8189**
Precip	GPCP	Global	0.7460	**0.7814**	0.7429	**0.7566**
Z500	JRA25	Global	0.9928	**0.9970**	**0.9951**	0.9943
SLP	JRA25	Global	0.9322	**0.9735**	0.9529	**0.9533**
T850	JRA25	Global	0.9949	**0.9950**	0.9908	**0.9943**
U850	JRA25	Global	0.9363	**0.9651**	**0.9435**	0.9401
U200	JRA25	Global	0.9580	**0.9702**	0.9648	**0.9778**
V200	JRA25	Global	0.8198	**0.8584**	0.7758	**0.8085**
Netrad	ERBE	Global	0.9577	**0.9714**	0.9499	**0.9644**
OLR	ERBE	Global	0.9387	**0.9503**	0.9425	**0.9539**
OSR	ERBE	Global	0.8778	**0.9076**	0.8550	**0.8873**
GZ5eddy	JRA25	Global	0.8918	**0.9145**	0.8108	**0.8503**
SLPeddy	JRA25	Global	0.9062	**0.9137**	0.8710	**0.8909**
T850eddy	JRA25	Global	0.9401	**0.9443**	0.9291	**0.9342**
U850eddy	JRA25	Global	0.8433	**0.8629**	0.8722	**0.9028**
U200eddy	JRA25	Global	0.8959	**0.9154**	0.8463	**0.9137**
Precip	TRMM-3B43	Tropics	0.7760	**0.8089**	0.7719	**0.7999**
Precip	CMAP	Tropics	0.7711	**0.8106**	0.7926	**0.8337**
Precip	GPCP	Tropics	0.7260	**0.7753**	0.7405	**0.7587**
Z500	JRA25	Tropics	**0.9679**	0.9621	0.9764	**0.9791**
SLP	JRA25	Tropics	0.9223	**0.9391**	0.9525	**0.9679**
T850	JRA25	Tropics	**0.9608**	0.9562	0.9718	**0.9798**
U850	JRA25	Tropics	0.8913	**0.9145**	0.9012	**0.9315**
U200	JRA25	Tropics	0.9644	**0.9707**	0.9723	**0.9885**
V200	JRA25	Tropics	0.8336	**0.8497**	0.8018	**0.8192**
GZ5eddy	JRA25	Tropics	**0.8258**	0.8243	0.8651	**0.9191**
SLPeddy	JRA25	Tropics	0.8225	**0.8615**	0.9127	**0.9438**
T850eddy	JRA25	Tropics	**0.8949**	0.8908	0.9274	**0.9454**
U850eddy	JRA25	Tropics	0.8406	**0.8565**	0.8827	**0.9180**
U200eddy	JRA25	Tropics	0.9028	**0.9218**	0.8768	**0.9390**

tology for the two versions of the model and observations. The vertically integrated moisture flux calculated from the JRA-25 reanalysis dataset is shown in Fig. 8a. Major convective centers over the eastern Arabian Sea, the Bay of Bengal, the South China Sea, the Philippine Sea, and southwest Japan are simulated well in v3.2. Compared with v3.1, precipitation is enhanced over South Asia and the western Pacific, while it decreases over the Arabian Sea, the western Bay of Bengal, the equatorial Indian Ocean, and the Maritime Continent (Fig. 8e). In addition to an improvement in simulating the rainfall amount over the western Pacific (see Section 4.1), v3.2 yields an improvement in the underestimated rainfall over northeastern India, as reported for the previous version of the model by Rajendran and Kitoh (2008). However, v3.2 still performs insufficiently in simulating a precipitation maximum on the southern coast of China (near 20°N, 110°E), which was reported for the previous version by Yatagai et al. (2005), and abundant rainfall around Bangladesh. The overall moisture-flux circulation field in v3.2 performs well in reproducing the observed features, with westerly fluxes over south Asia, easterly fluxes over the tropical Pacific Ocean, and southerly fluxes from the Philippines. Compared with v3.1, v3.2 shows a larger moisture flow over south Asia, penetrating into the

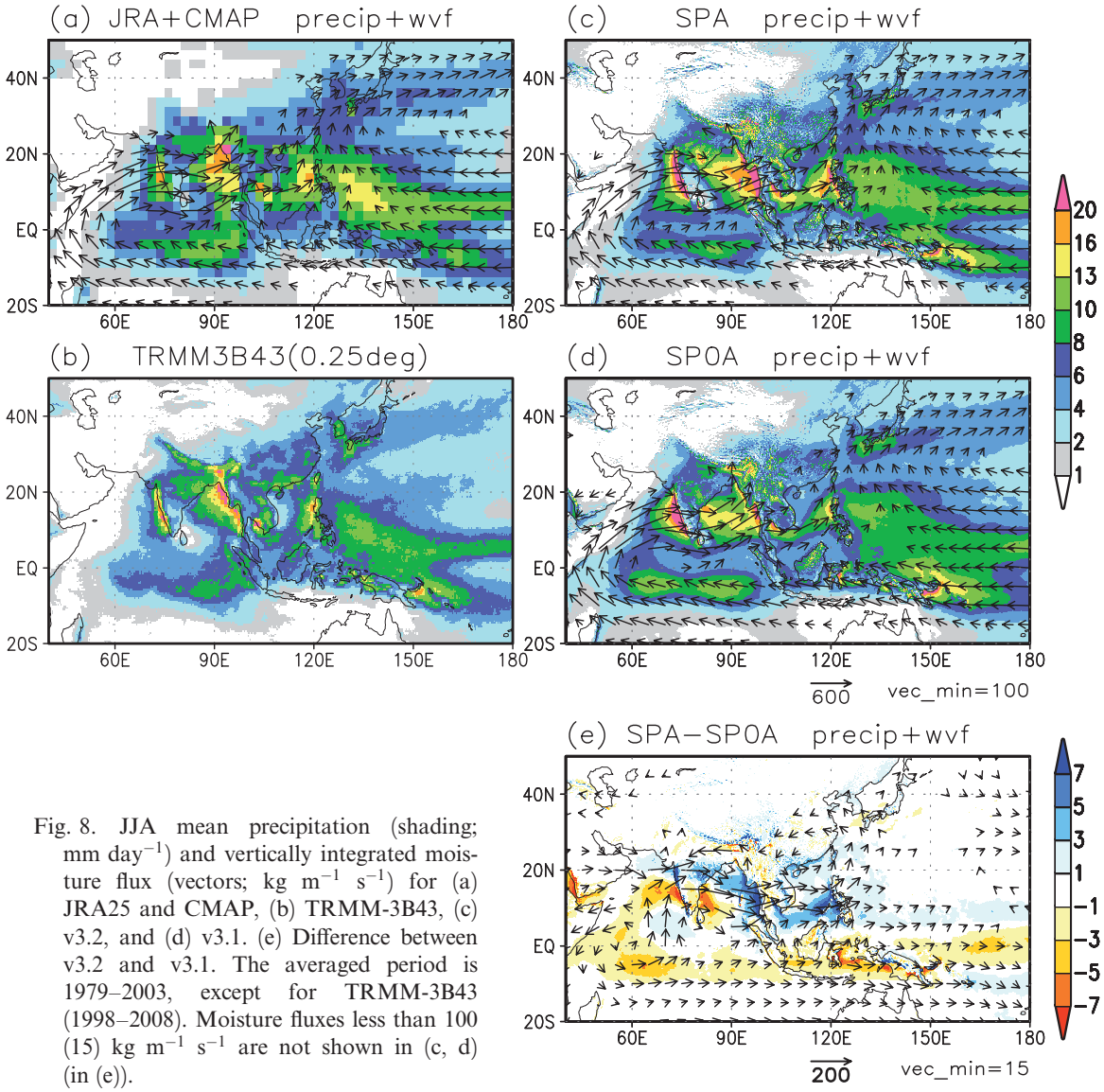

Fig. 8. JJA mean precipitation (shading; mm day^{-1}) and vertically integrated moisture flux (vectors; kg m^{-1} s^{-1}) for (a) JRA25 and CMAP, (b) TRMM-3B43, (c) v3.2, and (d) v3.1. (e) Difference between v3.2 and v3.1. The averaged period is 1979–2003, except for TRMM-3B43 (1998–2008). Moisture fluxes less than 100 (15) kg m^{-1} s^{-1} are not shown in (c, d) (in (e)).

Philippine Sea, which is in agreement with observations.

Figure 9 shows a Taylor's diagram over the Asian monsoon region (10°S–30°N, 40°E–160°E), for precipitation, zonal wind at 200 and 850 hPa, and meridional wind at 850 hPa, in order to make a quantitative comparison of performance between the two models. Improvements from v3.1 to v3.2 are seen for all the variables in terms of the skill score (Eq. 1). For precipitation, the standard deviation of its spatial distribution is larger than that for v3.1 and for observations. Averaged precipitation over the Asian monsoon region is 6.42 mm day^{-1} for v3.2, which is slightly less than that in v3.1 (6.53 mm day^{-1}), comparable with CMAP (6.27 mm day^{-1}), and larger than GPCP (5.34 mm day^{-1}).

To analyze the topography-regulated precipitation more clearly, Fig. 10 shows the zonal distribution of JJA mean precipitation averaged over 14°N–15°N. Observations indicate four precipitation peaks: west of the Western Ghats (74°E), west of Myanmar (98°E), west of the Annam Cordillera (107°E), and west of the Philippines (120°E). The locations of peak in v3.2 are in good agreement with observations, whereas v3.1 fails to simulate the peak located west of the Annam Cordillera and incorrectly reproduces a peak over the eastern Bay

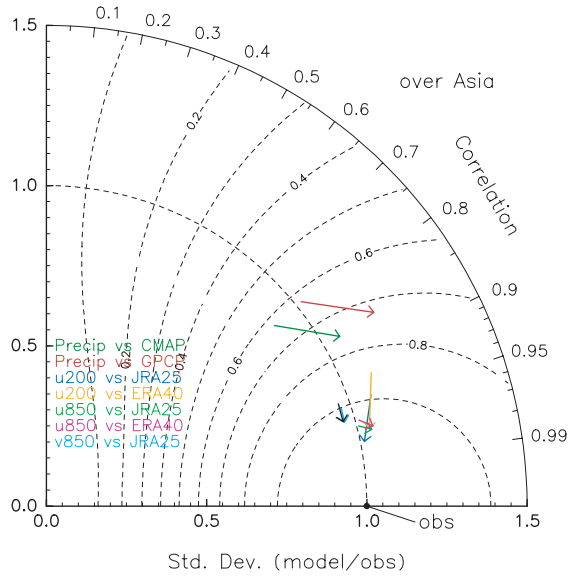

Fig. 9. Taylor diagram over the Asian monsoon region (10°S–30°N, 40°E–160°E) in JJA for the statistics for precipitation, zonal wind at 200 and 850 hPa, and meridional wind at 850 hPa. The statistics for v3.1 are plotted at the tail of arrows, and arrowheads point to the statistics for v3.2.

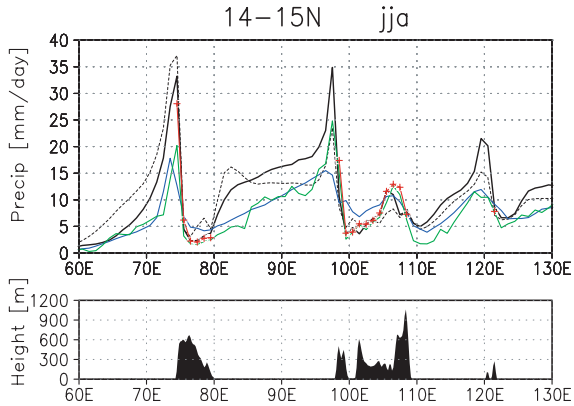

Fig. 10. JJA mean precipitation (mm day^{-1}) averaged over 14°N–15°N. Colors are as follows: GPCP (blue; Huffman et al. 2001), TRMM-3A25 (green), APHRODITE (red), v3.2 (solid black), and v3.1 (dashed black). Also shown is a topographic cross-section at the latitude. All data are displayed after interpolated onto a 1.0° grid. GPCP and TRMM-3A25 are averaged in 1997–2008.

of Bengal. Excessive precipitation in v3.1 over the area west of the Western Ghats and over the Arabian Sea is improved in v3.2. A gradual increase in precipitation toward the east over the Bay of Bengal is also simulated well in v3.2. In terms of precipitation amount over land, v3.2 yields similar values to APHRODITE; however, v3.2 shows excessive rainfall west of Myanmar and from the South China Sea to the Philippine Sea.

Figure 11 shows the seasonal evolution of the Asian monsoon, evaluated in terms of precipitation and wind fields. Figure 11a–c shows the area-averaged precipitation over three major monsoon regions: India and Bengal (Fig. 11a), the western North Pacific (Fig. 11b), and East Asia (Fig. 11c). In the India and Bengal region, v3.2 is able to reproduce the observed seasonal evolution (e.g., the sudden onset and gradual withdrawal of the monsoon), but it shows excessive rainfall in the warm season and a somewhat earlier onset. The same biases were reported in an intercomparison of 11 AGCMs (Wang et al. 2004). In the western North Pacific region, v3.2 performs well in simulating not only the seasonal evolution of rainfall, but also the amount, which is comparable to CMAP. However, neither model reproduces the observed sub-seasonal rainfall peak from late July to August.

Figure 11d shows the well-known wind shear index by Webster and Yang (1992), which measures broad-scale circulation associated with the South Asian monsoon. It is defined as zonal wind difference between at 850 hPa and 200 hPa over 0°N–20°N, 40°E–110°E. Also shown in Fig. 11e is each component of the index. The seasonal evolution of the wind shear index and each component are well simulated by v3.2, although with a slightly weak easterly in the upper troposphere during autumn. Figure 11f shows the western North Pacific monsoon index, defined by Wang et al. (2001) as the difference of 850 hPa zonal winds between 5°N–15°N, 100°E–130°E and 20°N–30°N, 110°E–140°E. It is an index of the circulation, which depicts large-scale vorticity of the monsoon trough over the western North Pacific in the lower troposphere. The monsoon trough in the warm season is slightly deeper in v3.2 compared with observations.

b. East Asian summer monsoon

Figure 11c shows the climatological seasonal cycle of precipitation over Japan (30°N–37.5°N, 125°E–145°E). There is little difference between the two observational data sets. The observations

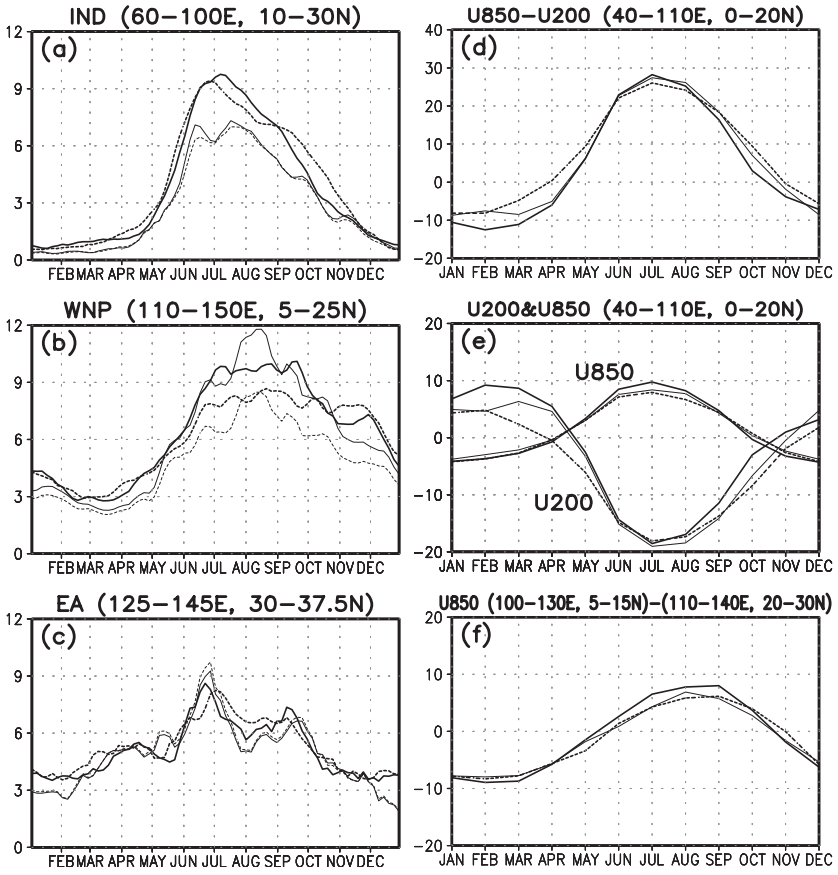

Fig. 11. Climatological seasonal cycle of three-pentad running mean precipitation (mm day^{-1}) averaged over (a) the Indian monsoon, (b) the western North Pacific monsoon, and (c) the East Asian monsoon region. Also shown is the climatological seasonal cycle of (d) the Webster-Yang index (Webster and Yang 1992), (e) each component of the index, and (f) the western North Pacific monsoon index (Wang et al. 2001) based on monthly mean data. The v3.2 (v3.1) model is shown by a thick solid (thick dashed) line. CMAP (GPCP) is shown by a thin solid (thin dashed) line in (a–c). JRA-25 is shown by a thin solid line in (d–f).

show two rainfall peaks: a distinct peak in early summer, called the Baiu (Ninomiya and Akiyama 1992), and a peak in early autumn, called the Shurin (Matsumoto 1988). The period between the two peaks (late July to August) is relatively dry. Thus, the seasonal cycle in the warm season over Japan shows complexities at the subseasonal scale. Nevertheless, v3.2 is successful in simulating the characteristic features of the seasonal cycle; i.e., it correctly reproduces the peak and break timing, and the precipitation amount.

Figure 12 shows the mean precipitation, sea level pressure, and zonal wind speed at 200 hPa from June through September. Observations (Fig. 12a) show a narrow rain band at around 30°N in June. The North Pacific anticyclone expands westward on the southern side of the rain band, and westerly jet at upper troposphere is located slightly north of the rain band. The rain band, the anticyclone, and the westerly jet migrate northward with the seasonal progress in early summer, becoming gradually weaker. In August, the anticyclone expands northwestward, prevailing over Japan and bringing rainfall to north China with a southerly wind. In September, the rain band and the westerly jet migrate southward and become strong again, and the anticyclone is located over the Pacific east of Japan. These large-scale features of the complex seasonal march in East Asia are well captured by v3.2 (Fig. 12b), whereas v3.1 cannot reproduce the relatively dry spell around Japan in August (Fig. 12c), which is also shown in Fig. 11c. In v3.2, however, the

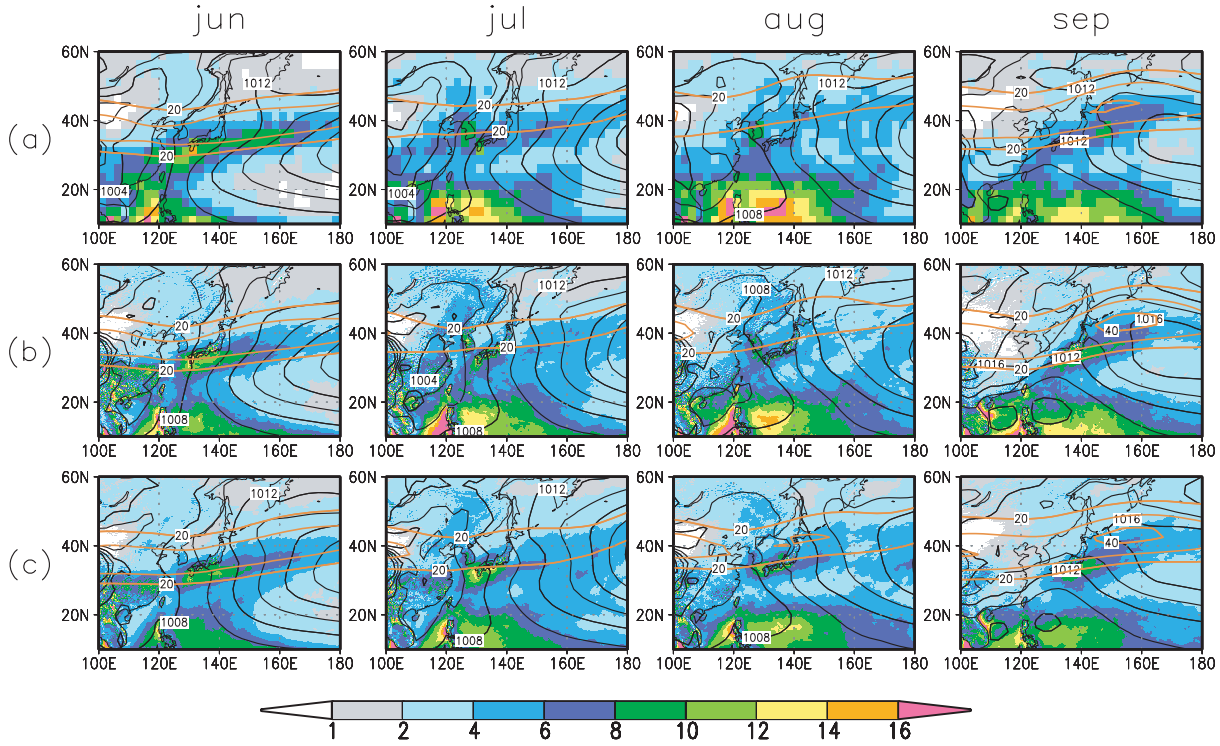

Fig. 12. Climatological monthly mean field in (a) JRA and CMAP, (b) v3.2, and (c) v3.1 from June to September. Black contours: sea level pressure (hPa, contour interval is 2 hPa). Thick orange contours: zonal wind speed at 200 hPa (m s^{-1}, contour interval is 10 m s^{-1}, and contours for values less than 20 m s^{-1} are omitted). Shading: precipitation (mm day^{-1}).

westward extension of the anticyclone is still slightly weak in early summer.

c. *Intraseasonal variability*

Intraseasonal variability (ISV) simulated by v3.2 is investigated and compared to observation as well as to v3.1. Previous studies reported that tropical intraseasonal variability such as the Madden-Julian oscillation (MJO) in the previous version of the model is not so realistic, which simulated low amplitudes in convection and low-level winds in the 30–60-day band and showed standing oscillation (Rajendran et al. 2008; Liu et al. 2009).

Figure 13 shows wavenumber-frequency spectra of precipitation and 850 hPa zonal wind (U850) along the equator (10°N–10°S mean) during boreal winter (November to April). In observation, the power is concentrated at 30–80 days and at zonal wavenumbers 1–3 for precipitation and at zonal wavenumber 1 for U850. V3.2 improves the power spectra in low frequency band compared to v3.1. However, the spectral power in the MJO band is still weaker than the observation, and the simulated power is distributed more in the time periods longer than 90 days.

In boreal summer, observations show the ISV propagates northward as well as eastward in south Asia (Wang and Rui 1990). In order to show the space-time variability associated with boreal summer intraseasonal variability (BSISV), distinct BSISV events are composited based on the extended empirical orthogonal function (EEOF) analysis following Waliser et al. (2003). The EEOF analysis includes 60°E–180°E and 30°S–30°N domain and −4 to +5 pentad lags in 20–90-day filtered precipitation anomaly (from climatology) from May to September. The events are selected based on the first EEOF time series having peak values exceeding 1.0 standard deviation. The number of selected events is 38 in the observation, 30 in v3.2, and 29 in v3.1.

Figure 14 shows the composited time evolution of the BSISV events in the models and the observation. The observation shows northward propaga-

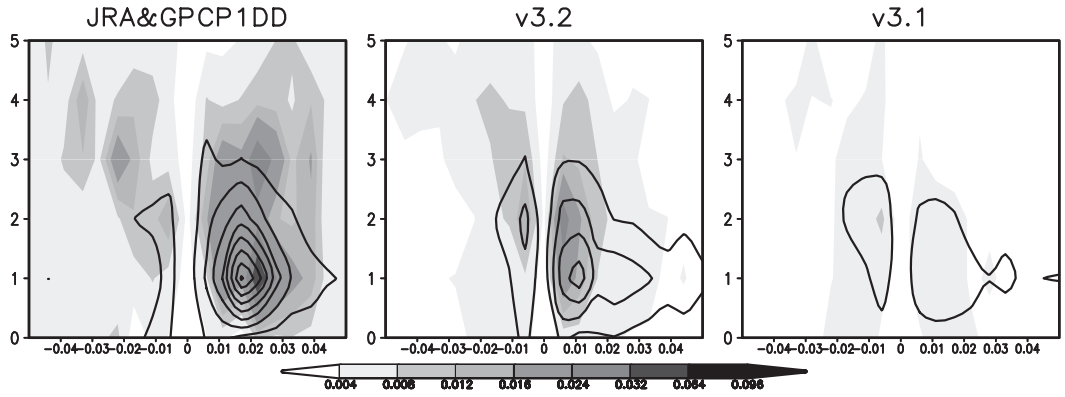

Fig. 13. Wavenumber-frequency spectra of 10°N–10°S averaged precipitation (shade; $mm^2\ day^{-2}$) and 850 hPa zonal wind (contour; $m^2\ s^{-2}$) along the equator (10°N–10°S mean) during boreal winter (November to April), for (left) JRA25 and GPCP, (center) v3.2, and (right) v3.1. Horizontal axis shows frequency (day^{-1}) and vertical axis shows zonal wave number. Counter interval is 0.01 $m^2\ s^{-2}$.

tion of intraseasonal precipitation anomalies from the equator with the northwest-southeast tilted band as documented by many previous studies (e.g., Wang and Rui 1990; Waliser et al. 2003). The feature is reproduced realistically to some extent, although the amplitude over the equatorial eastern Indian Ocean remains smaller compared with the observation. On the contrary, v3.1 does not reproduce the feature at all.

4.3 Inter-annual variability

Interannual variations in tropical precipitation are compared with observations using an empirical orthogonal function (EOF) analysis. Figure 15 shows the leading eigenvectors of JJA and DJF mean precipitation over the tropics (30°S–30°N). The precipitation for GPCP and the models is interpolated on a common 2.5° grid, and an EOF analysis is applied. The first leading modes in both JJA and DJF are associated with ENSO: the correlation coefficient between the principal component of the first mode and SST over the Nino3.4 region is 0.92 in JJA and 0.94 in DJF. In JJA, the first mode in the observations and the models explains about 20% of the total variance. V3.2 improves the spatial pattern of the first mode (e.g., over the equatorial Indian Ocean, Southeast Asia, and the Philippine Sea). Kitoh and Kusunoki (2008) reported that v3.1 has less skill in simulating the anomaly of the first mode over the Philippine Sea. In DJF, the first mode in the observations and the models explains more than 30% of the total variance. Contrasting zonal anomalies over the Maritime Continent and the equatorial Pacific are successfully produced in v3.2, whereas v3.1 fails to simulate these anomalies and shows the dominance of meridionally contrasting anomalies over the equatorial Pacific. Kang et al. (2004) reported that most AGCMs have difficulty in simulating the negative anomalies over the Maritime Continent during the winter of 1997/98, based on an intercomparison of AMIP-type experiments with 11 AGCMs. A band-shaped anomaly over southern China is also well simulated in v3.2. The spatial correlation coefficient in the first mode between the observations and the models is 0.78 in JJA and 0.89 in DJF for v3.2, while 0.63 in JJA and 0.75 in DJF for v3.1. It is noted that the first-mode pattern over the Asian–Australian monsoon region is greatly improved in v3.2, despite the use of an AMIP-type simulation without air–sea interaction.

4.4 Precipitation intensity

To simulate geographical distributions of extreme precipitation events such as heavy rainfall or severe drought and their future change, the frequency of heavy precipitation as well as time-averaged amount must be simulated in the model. Kamiguchi et al. (2006) reported that the previous version of the model overestimates the frequency of weak rain, and underestimates the frequency of heavy rain, especially in low latitudes. Here, the probability distribution functions (PDFs) of daily precipitation are compared with observations. Figure 16 shows the PDFs of daily precipitation in JJA for regions of low latitudes (30°S–30°N), middle latitudes (30°N–40°N), India (80°E–90°E, 5°N–30°N), Indochina (95°E–110°E, 0–20°N),

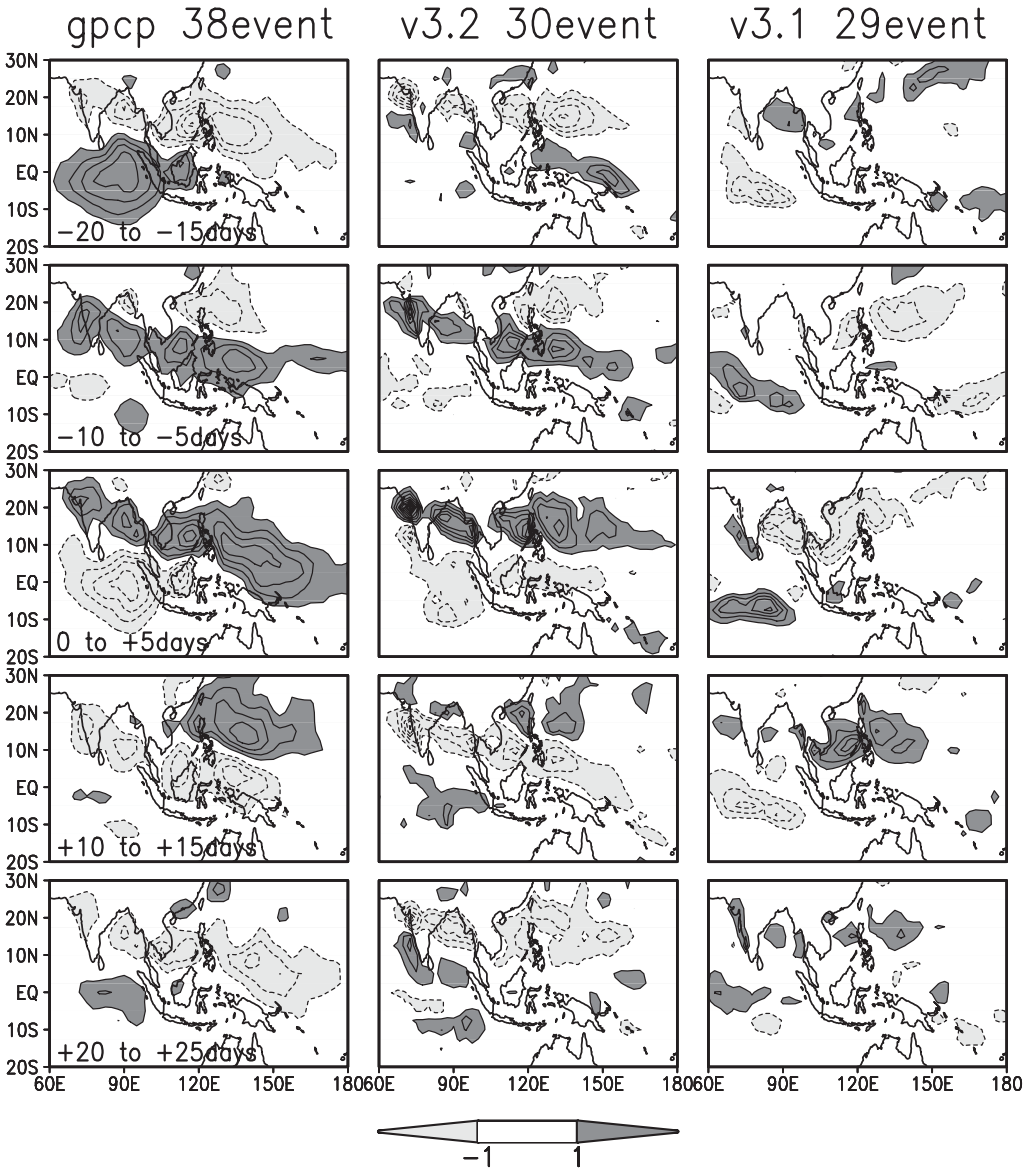

Fig. 14. Composited time evolution for distinct events of boreal summer intraseasonal variability in terms of 20–90-day filtered precipitation (anomaly from climatology) from May to September in (left) GPCP, (middle) v3.2 and (right) v3.1. Contour interval is 1 mm day^{-1}. The events are identified using an extended EOF (EEOF) analysis (see the text for details).

Borneo (109°E–110°E, 4°S–6°N), and South Japan (129°E–146°E, 30°N–40°N). All the data is re-gridded to a 1° grid. The frequency of heavy rain more than 40 mm day^{-1} becomes higher in v3.2 than that in v3.1 for all regions. For low latitudes (Fig. 16a, c, d, e), the frequency of heavy rain in v3.2 comes between that in GPCP and that in TRMM-3B42 except for Borneo (Fig. 16e). The frequency of weak rain less than 15 mm day^{-1} is still overestimated even if the observational uncertainty is taken into account, although the overestimation is improved in v3.2. For mid latitudes (Fig. 16b) and Japan (Fig. 16f), the PDFs are between the two observations in v3.2 as well as v3.1. The PDF in v3.2 is closer to TRMM-3B42 compared with that in v3.1.

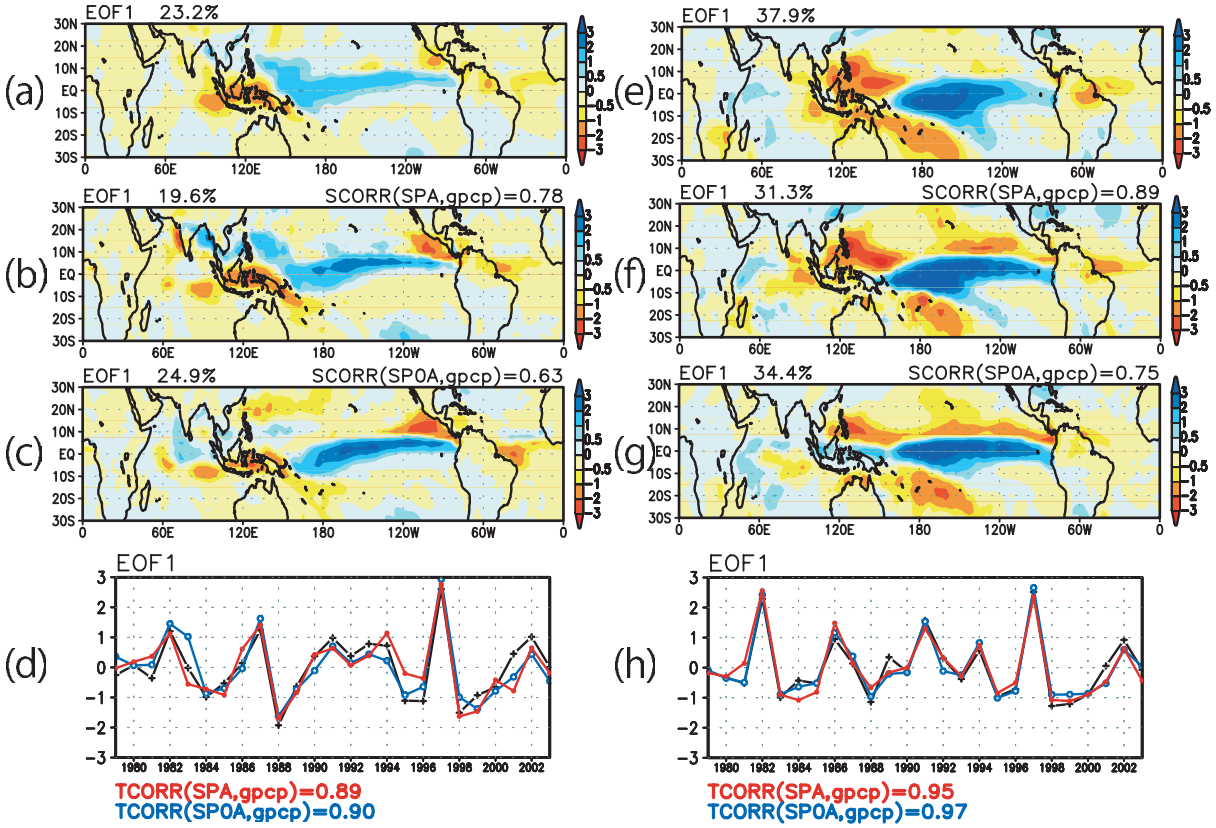

Fig. 15. The leading EOF mode in the tropics (30°S–30°N) based on (a–d) the JJA mean precipitation (mm day^{-1}) and (e–h) the DJF mean precipitation for the period 1979–2003 for (a, e) GPCP, (b, f) v3.2, and (c, g) v3.1. (d,h) EOF coefficients for GPCP (black), v3.2 (red), and v3.1 (blue). The EOF modes are normalized in order that its time coefficients have one standard deviation.

4.5 *Tropical cyclones*

The climatological features of tropical cyclones (TCs) are significantly improved in v3.2. This section describes some of these improvements. Details will be discussed in separate publications.

Self-organized TCs in the models are detected using the same method and threshold values as those used in Oouchi et al. (2006), which use six criteria on (1) the minimum surface pressure relative to the surrounding 7° grid box, (2) the maximum relative vorticity at 850 hPa, (3) the maximum wind speed at 850 hPa, (4) the sum of the temperature deviations at 300, 500 and 700 hPa, (5) the maximum wind speed at 850 hPa relative to that at 300 hPa, and (6) the duration time. The threshold values for the criteria are intended to make the global TC frequency in v3.1 comparable to the observed annual frequency (about 80 TCs per year). Table 3 shows the ratio of the annual mean TC genesis number for each basin relative to the global mean number, by v3.2, v3.1, and the observational "best track" data provided by Unisys (2011). A significant improvement is seen in the western North Pacific (WNP), where a lower ratio of TCs was detected in v3.1 (Murakami and Sugi 2010; Murakami et al. 2011). This improvement is consistent with the increase in monthly precipitation in this area. Improvements are also seen in most other regions, except for the North Indian Ocean. However, considering that the TC ratio in the North Indian Ocean is relatively small compared with other ocean basins, the global distribution of TCs is significantly improved.

Figure 17 shows the probability density of the life-cycle maximum surface wind speed over the global domain. In v3.1, TC intensity is largely underestimated compared with observations. Although the question of how realistically the 20-km-mesh model should reproduce the observed TC intensity is a topic for debate, v3.1 is too weak in

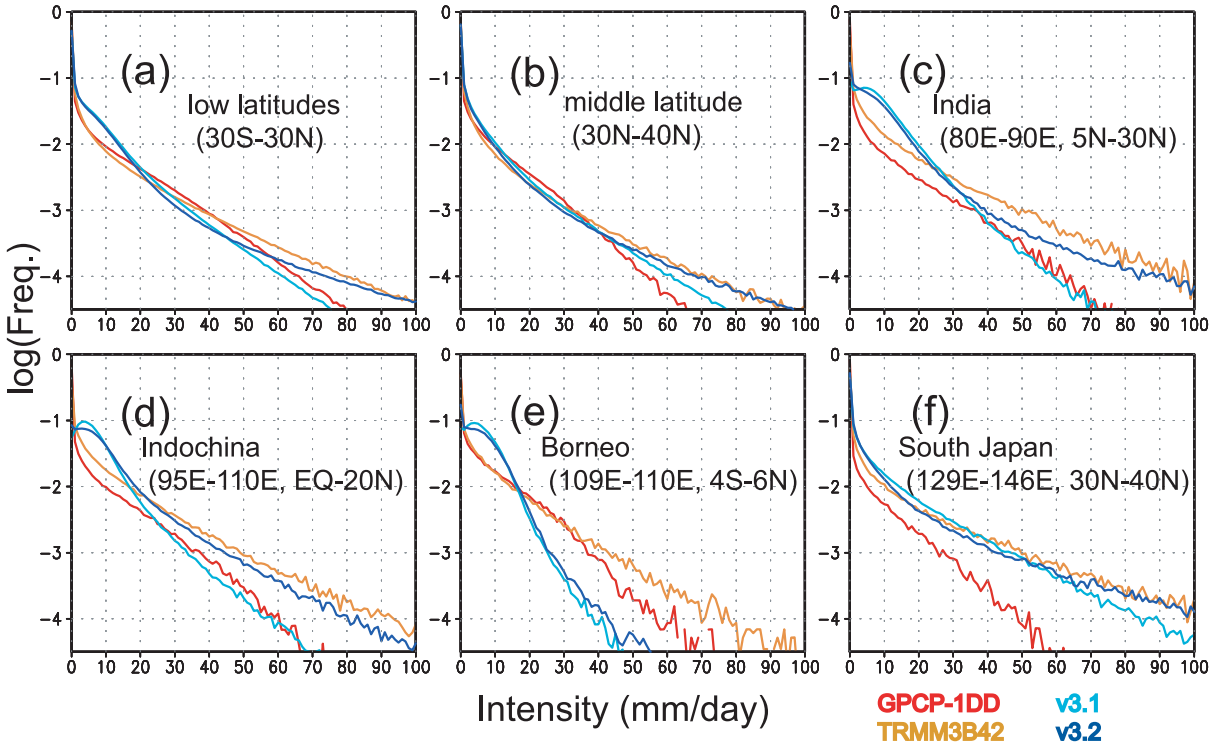

Fig. 16. Probability distribution functions of daily precipitation in JJA in regions of (a) low latitudes (30°S–30°N), (b) middle latitudes (30°N–40°N), (c) India (80°E–90°E, 5°N–30°N), (d) Indochina (95°E–110°E, 0°N–20°N), (e) Borneo (109°E–110°E, 4°S–6°N), and (f) South Japan (129°E–146°E, 30°N–40°N). The v3.2 (v3.1) model is shown by a blue (green) line. GPCP (TRMM-3B42) is shown by a red (orange) line.

Table 3. Ratio of the annual mean tropical-cyclone genesis number for each basin (percent) relative to the global mean number during the period 1979–2003, by v3.2, v3.1, and observational best track data. Bold entries denote an overestimation by more than 5%, and italics denote an underestimation by more than 5%.

	N. Indian	N.W. Pacific	E. Pacific	N. Atlantic	S. Indian	S. Pacific	RMSE
v3.2	*11.2*	26.6	20.1	8.3	18.4	14.7	3.8
v3.1	5.5	**21.0**	*25.4*	7.5	*25.2*	*15.1*	6.2
Observed	4.6	26.9	16.7	10.5	16.0	10.0	

terms of intensity when the results are compared with other modeling studies with coarser resolutions (e.g., Fig. 6 of Zhao et al. (2009), who used a 60-km-mesh model). TC intensity is also significantly improved in v3.2: stronger TCs with a higher maximum wind speed (more than 50 m s^{-1}) are better simulated in v3.2 compared with v3.1.

4.6 *Extratropics*

As an index of synoptic activity over the extratropics, Fig. 18 shows the zonal-mean 2–8-day eddy kinetic energy on 300 hPa for 25 years of boreal winter, for JRA25, v3.2, and v3.1. Shading denotes the model bias from JRA25. We used the velocity data interpolated onto a 1.25° grid for the models and the reanalysis. Positive biases around the eastern Pacific and from the eastern Atlantic to Europe, as seen in v3.1 (Fig. 18c), are reduced in v3.2 (Fig. 18b). However, a positive bias is seen on the southern side of the Atlantic storm track in v3.2. In both v3.1 and v3.2, activity is higher around the eastern Mediterranean sea and smaller around southern Siberia, compared with the reanalysis.

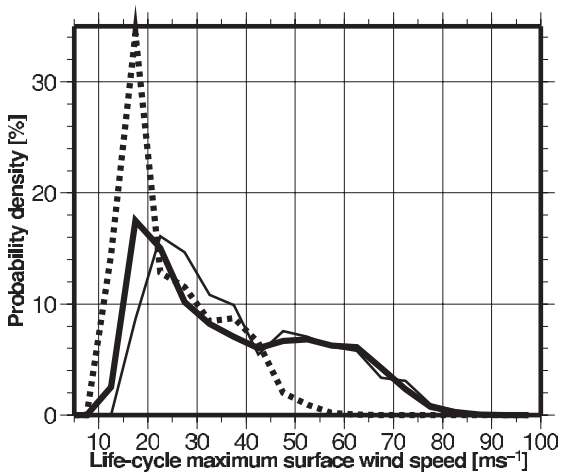

Fig. 17. Probability density of the life-cycle maximum surface wind speed (m s^{-1}) for the global domain during the period 1979–2003 for observational best track data (thin solid line), v3.2 (thick solid line), and v3.1 (thick dashed line). Bin widths are 5 m s^{-1}.

Figure 19 shows a Hovmöller diagram of climatological annual cycle of blocking frequency in the Northern Hemisphere for the period 1979–2003. Occurrence of blocking is defined by using the objective blocking index based on D'Andrea et al. (1998). There are well-known blocking maxima over the Euro-Atlantic region (30°W–70°E) from winter to summer, and over the Pacific region (120°E–120°W) in winter and summer. The frequency and seasonal variations of Euro-Atlantic blocking are simulated well in v3.2, but encounters difficulty in simulating the Ural blocking frequency (50°E–70°E) in JJA. The Pacific blocking frequency in winter is overestimated in v3.2 as well as in v3.1 (Matsueda et al. 2009). The Pacific blocking in summer, especially the Western Pacific blocking (120°E–180°E), remains underestimated in v3.2.

5. Summary and discussion

We have developed MRI-AGCM3.2, a new version of the atmospheric general circulation model of the Meteorological Research Institute, with a horizontal grid size of 20 km. Various new parameterization schemes have been introduced to improve the simulation of the present climate. An AMIP-type climate experiment was performed for 25 years using the new model (v3.2), and the results are compared with those of the same experiment conducted using the previous version of the model (v3.1).

Improvements are seen in v3.2 in simulating the monthly-mean precipitation (Fig. 2), especially heavy precipitation around the tropical Western Pacific during boreal summer (Fig. 8). Zonal-mean temperature and zonal wind (Fig. 5), and other seasonal-mean climatologies are also improved, which are confirmed numerically using Taylor's skill score (Table 2 and Fig. 7).

By virtue of the high resolution, topography-regulated precipitation has better agreement with observations, as shown in Asia from India to the Philippines (Fig. 10). Seasonal evolution of the Asian monsoon is well simulated in the model (Fig. 11). In particular, v3.2 is successful in simulating the characteristic features of the seasonal cycle of the East Asian summer monsoon (Fig. 12).

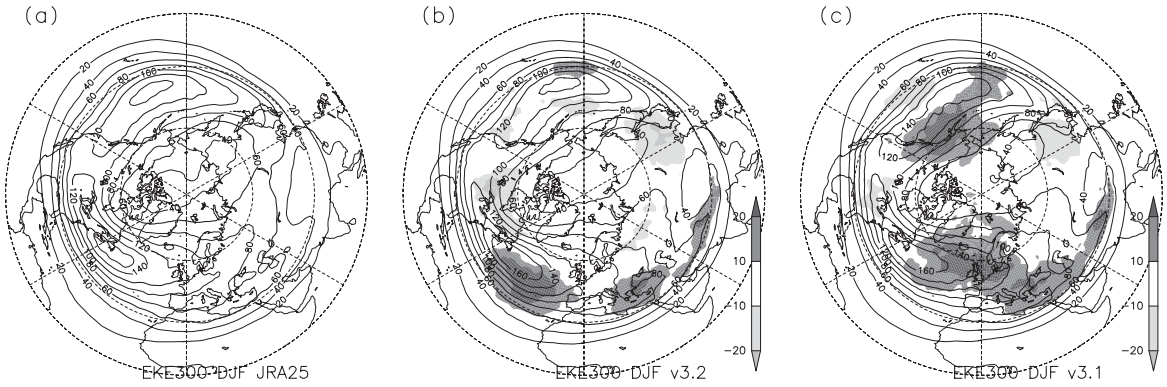

Fig. 18. Zonal-mean 2–8-day eddy kinetic energy (m^2 s^{-2}) on 300 hPa for 25 years of DJF for (a) JRA25, (b) v3.2, and (c) v3.1. Shading in (b) and (c) indicates difference from JRA25.

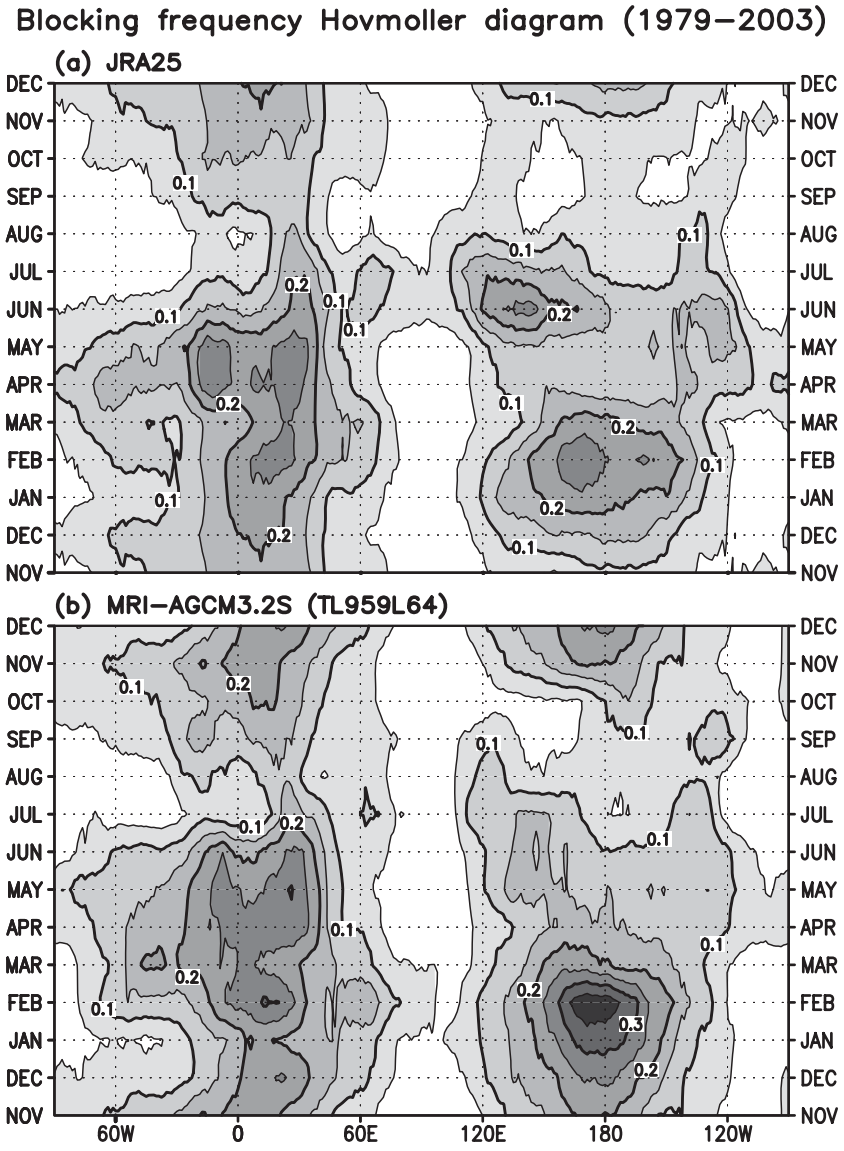

Fig. 19. Hovmöller diagrams of climatological annual cycle of blocking frequency for (top) JRA25 and (bottom) v3.2 during the period 1979–2003.

Improvements are also found in the inter-annual variability of tropical precipitation (Fig. 15), and the global distribution and intensity of tropical cyclones (Table 3 and Fig. 17). Although tropical intraseasonal variability (Figs. 13, 14), precipitation intensity (Fig. 16), and extratropical storm tracks (Fig. 18) also show better performance to some extent, more detailed investigation from many different perspectives would be required to produce a more realistic simulation in the model.

The introduction of a new cumulus parameterization scheme contributed to these improvements, especially in terms of precipitation around the tropical Western Pacific and tropical cyclones. Weak precipitation is more frequent in v3.1 than that observed (Fig. 16), associated with a tendency of the Arakawa–Schubert scheme used in v3.1 to resolve instability faster and to readily reduce the convective available potential energy (CAPE), even under dry atmospheric conditions. In v3.2, CAPE is maintained at a higher level (E. Shindo 2010, personal communication), associated with the change

that the new cumulus scheme includes turbulent entrainment and turbulent detrainment, unlike the Arakawa–Schubert scheme. Cloud top in the tropics generally becomes lower, and more heat and moisture are supplied to the middle troposphere (E. Shindo 2010, personal communication). Corresponding to these changes, weak precipitation becomes less frequent, and convection is more frequently organized into the scale of tropical cyclones. Moreover, moisture transport from the Indian Ocean to the Western Pacific has been enhanced, which might lead in turn to the enhanced precipitation in the tropical Western Pacific.

Tropical intraseasonal variability in the previous version of the model (e.g., Madden–Julian oscillation; MJO) has a much weaker amplitude than that observed (Rajendran et al. 2008; Liu et al. 2009). Although the variance in v3.2 is larger than that in v3.1 (Fig. 13), it appears to be insufficient compared with observations. Moistening of the middle troposphere by the change in the cumulus parameterization could contribute to the larger amplitude. A higher-resolution cloud-resolving model is able to simulate intraseasonal variability. Miura et al. (2007) showed that a global cloud-resolving model with a horizontal resolution of 7 km is able to simulate the slow eastward migration of an MJO event. Even when using hydrostatic models with cumulus parameterization, a realistic amplitude of MJO can be simulated by improving the parameterization scheme (Bechtold et al. 2008). The task of obtaining a more realistic simulation of intraseasonal variability remains a topic for future study under a similar framework to that of the current model.

We have already performed future climate experiments using v3.2. Two time-slice 25-year simulations, corresponding to the near future (2015–2039) and at the end of the 21st century (2075–2099), were performed using boundary SST data derived by superposing the future change in the ensemble of SST projected by the CMIP3 multi-model dataset on the observed SST. The future climate change in this high-resolution model, using the difference between these results and the results of the present study, will be reported in subsequent publications.

Acknowledgements

The development of the model is based on the work of many people, especially those in the Numerical Prediction Division of JMA and in the development team of MRI-ESM. This work was conducted under the framework of the ''Projection of the Change in Future Weather Extremes using Super-high-resolution Atmospheric Models'' supported by the KAKUSHIN Program of the Ministry of Education, Culture, Sports, Science, and Technology. The calculations were performed on the Earth Simulator. We thank the U.S. CLIVAR MJO Working Group for providing the software package, which is used to depict Fig. 13. We also thank two anonymous reviewers for constructive comments.

References

Adler, R. F., G. J. Huffman, A. Chang, R. Ferrano, P.-P. Xie, J. Janowiak, B. Rudolf, U. Schneider, S. Curtis, D. Bolvin, A. Gruber, J. Susskind, P. Arkin, and E. Nelkin, 2003: The version–2 global precipitation climatology preject (GPCP) monthly precipitation analysis (1979–present). *J. Hydrometeor.*, **4**, 1147–1167.

Arakawa, A., and W. H. Schubert, 1974: Interaction of cumulus cloud ensemble with the large-scale environment. Part I. *J. Atmos. Sci.*, **31**, 674–701, doi:10.1175/1520-0469(1974)031〈0674:IOACCE〉2.0.CO;2.

Bourke, R. H., and R. P. Garrett, 1987: Sea ice thickness distribution in the Arctic Ocean. *Cold Regions Sci. and Tech.*, **13**, 259–280, doi:10.1016/0165-232X(87)90007-3.

Bechtold, P., M. Köhler, T. Jung, F. Doblas-Reyes, M. Leutbecher, M. J. Rodwell, F. Vitart, and G. Balsamo, 2008: Advances in simulating atmospheric variability with the ECMWF model: From synoptic to decadal time-scales. *Quart. J. Roy. Meteor. Soc.*, **134**, 1337–1351, doi: 10.1002/qj.289.

Chin, M., P. Ginoux, S. Kinne, O. Torres, B. N. Holben, B. N. Duncan, R. V. Martin, J. A. Logan, A. Higurashi, and T. Nakajima, 2002: Tropospheric aerosol optical thickness from the GOCART model and comparisons with satellite and sun photometer measurements. *J. Atmos. Sci.*, **59**, 461–483.

D'Andrea, F., S. Tibaldi, M. Blackburn, G. Boer, M. Déqué, M. R. Dix, B. Dugas, L. Ferranti, T. Iwasaki, A. Kitoh, V. Pope, D. Randall, E. Roeckner, D. Straus, W. Stern, H. Van den Dool, and D. Williamson, 1998: Northern Hemisphere atmospheric blocking as simulated by 15 atmospheric general circulation models in the period 1979–1988. *Clim. Dyn.*, **14**, 385–407.

Eyring,V., N. R. P. Harris, M. Rex, T. G. Shepherd, D. W. Fahey, G. T. Amanatidis, J. Austin, M. P. Chipperfield, M. Dameris, P. M. De F. Forster, A. Gettelman, H. F. Graf, T. Nagashima, P. A.

Newman, S. Pawson, M. J. Prather, J. A. Pyle, R. J. Salawitch, B. D. Santer, and D. W. Waugh, 2005: A strategy for process-oriented validation of coupled chemistry-climate models. *Bull. Amer. Meteor. Soc.*, **86**, 1117–1133.

European Centre for Medium-Range Weather Forecasts, 2004: IFS Documentation CY28r1. (Available online at: http://www.ecmwf.int/research/ifsdocs/CY28r1/index.html).

European Centre for Medium-Range Weather Forecasts, 2009: IFS Documentation CY33r1. (Available online at: http://www.ecmwf.int/research/ifsdocs/CY33r1/index.html).

Harrison, E. F., P. Minnis, B. R. Barkstrom, V. Ramanathan, R. D. Cess, and G. G. Gibson, 1990: Seasonal variation of cloud radiative forcing derived from the Earth Radiation Budget Experiment. *J. Geophys. Res.*, **95**, 18,687–18,703.

Hess, M., P. Koepke, and I. Schult, 1998: Optical properties of aerosols and clouds: The software package OPAC. *Bull. Amer. Meteor. Soc.*, **79**, 831–844.

Hirai, M., T. Sakashita, H. Kitagawa, T. Tsuyuki, M. Hosaka, and M. Oh'izumi, 2007: Development and validation of a new land surface model for JMA's operational global model using the CEOP observation dataset. *J. Meteor. Soc. Japan*, **85A**, 1–24.

Huffman, G. J., R. F. Adler, M. M. Morrissey, D. T. Bolvin, S. Curtis, R. Joyce, B. McGavock, and J. Susskind, 2001: Global precipitation at one-degree daily resolution from multi-satellite observations. *J. Hydrometeor.*, **2**, 36–50.

Huffman, G. J., R. F. Adler, D. T. Bolvin, G. Gu, E. J. Nelkin, K. P. Bowman, E. F. Stocker, and D. B. Wolff, 2007: The TRMM multisatellite precipitation analysis (TMPA): Quasi-global, multiyear, combined-sensor precipitation estimates at fine scale. *J. Hydrometeor.*, **8**, 38–55.

Iguchi, T., T. Kozu, R. Meneghini, J. Awaka, and K. Okamoto, 2000: Rainprofiling algorithm for the TRMM Precipitation Radar. *J Appl. Meteor.*, **39**, 2038–2052.

Iwasaki, T., S. Yamada, and K. Tada, 1989: A parameterization scheme of orographic gravity wave drag with the different vertical partitioning, part 1: Impact on medium range forcast. *J. Meteor. Soc. Japan*, **67**, 11–41.

Jakob, C., 2001: The representation of cloud cover in atmospheric general circulation models. PhD thesis, Ludwig-Maximilians-Universitaet Muenchen, 193 pp.

Japan Meteorological Agency, 2007: *Outline of the operational numerical weather prediction at the Japan Meteorological Agency (Appendix to WMO numerical weather prediction progress report)*. Japan Meteorological Agency, 194 pp. (Available online at http://www.jma.go.jp/jma/jma-eng/jma-center/nwp/outline-nwp/index.htm).

Jin, F. J., A. Kitoh, and P. Alpert, 2010: Water cycle changes over the Mediterranean: A comparison study of a super-high-resolution global model with CMIP3. *Phil. Trans. R. Soc. A*, **368**, 1–13.

Kamiguchi, K., A. Kitoh, T. Uchiyama, R. Mizuta, and A. Noda, 2006: Changes in precipitation-based extremes indices due to global warming projected by a global 20-km-mesh atmospheric model. *SOLA*, **2**, 64–67, doi:10.2151/sola.2006-017.

Kanada, S., M. Nakano, and T. Kato, 2010: Changes in mean atmospheric structures around Japan during July due to global warming in regional climate experiments using a cloud-system resolving model. *Hydrological Research Letters*, **4**, 11–14, doi:10.3178/HRL.4.11.

Kanamitsu, T., K. Tada, T. Kudo, N. Sato, and S. Isa, 1983: Description of the JMA operational spectral model. *J. Meteor. Soc. Japan*, **61**, 812–828.

Kang, I.-S., K. Jin, B. Wang, K.-M. Lau, J. Shukla, V. Krishnamurthy, S. D. Schubert, D. E. Wailser, W. F. Stern, A. Kitoh, G. A. Meehl, M. Kanamitsu, V. Y. Galin, V. Satyan, C.-K. Park, and Y. Liu, 2002: Intercomparison of the climatological variations of Asian summer monsoon precipitation simulated by 10 GCMs. *Clim. Dyn.*, **19**, 383–395, doi:10.1007/s00382-002-0245-9.

Kawai, H., 2006: PDF cloud scheme and prognostic cloud scheme in JMA global model. *CAS/JSC WGNE Research Activities in Atmospheric and Ocean Modeling*, **36**, 4.15–4.16.

Kitoh, A., and S. Kusunoki, 2008: East Asian summer monsoon simulation by a 20-km mesh AGCM. *Clim. Dyn.*, **31**, 389–401, doi:10.1007/s00382-007-0285-2.

Kitoh, A., T. Ose, K. Kurihara, S. Kusunoki, M. Sugi, and KAKUSHIN Team-3 Modeling Group, 2009: Projection of changes in future weather extremes using super-high-resolution global and regional atmospheric models in the KAKUSHIN Program: Results of preliminary experiments. *Hydrological Research Letters*, **3**, 49–53, doi:10.3178/hrl.3.49.

Kusunoki, S., J. Yoshimura, H. Yoshimura, A. Noda, K. Oouchi, and R. Mizuta, 2006: Change of Baiu rain band in global warming projection by an atmospheric general circulation model with a 20-km grid size. *J. Meteor. Soc. Japan*, **84**, 581–611.

Liu, P., Y. Kajikawa, B. Wang, A. Kitoh, T. Yasunari, T. Li, H. Annamalai, X. Fu, K. Kikuchi, R. Mizuta, K. Rajendran, D. E. Waliser, and D. Kim, 2009: Tropical intraseasonal variability in the MRI-20km60L AGCM. *J. Climate*, **22**, 2006–2022, doi:10.1175/2008JCLI2406.1.

Matsueda, M., R. Mizuta, and S. Kusunoki, 2009: Future change in wintertime atmospheric blocking

simulated using a 20-km-mesh atmospheric global circulation model. *J. Geophys. Res.*, **114**, D12114, doi:10.1029/2009JD011919.

Matsumoto, J., 1988: Large-scale features associated with the frontal zone over East Asia from late summer to autumn. *J. Meteor. Soc. Japan*, **66**, 565–579.

McFarquhar, G. M., S. Iacobellis, and R. C. J. Somerville, 2003: SCM simulations of tropical ice clouds using observationally based parameterizations of microphysics. *J. Climate*, **16**, 1643–1664.

Mellor, G. L., and T. Yamada, 1974: A hierarchy of turbulence closure models for planetary boundary layers. *J. Atmos. Sci.*, **31**, 1791–1806.

Miura, H., M. Satoh, T. Nasuno, A. T. Noda, and K. Oouchi, 2007: A Madden-Julian Oscillation event simulated using a global cloud-resolving model. *Science*, **318**, 1763–1765, doi:10.1126/science.1148443.

Mizuta, R., K. Oouchi, H. Yoshimura, A. Noda, K. Katayama, S. Yukimoto, M. Hosaka, S. Kusunoki, H. Kawai, and M. Nakagawa, 2006: 20-km-mesh global climate simulations using JMA-GSM model—mean climate states—. *J. Meteor. Soc. Japan*, **84**, 165–185, doi:10.2151/jmsj.84.165.

Murakami, H., B. Wang, and A. Kitoh, 2011: Future change of western North Pacific typhoons: Projections by a 20-km-mesh global atmospheric model. *J. Climate*, in press.

Murakami, H., and M. Sugi, 2010: Effect of model resolution on tropical cyclone climate projections. *SOLA*, **6**, 73–76, doi:10.2151/sola.2010-019.

Nakaegawa, T., and W. Vergara, 2010: First projection of climatological mean river discharges in the magdalena river basin, Colombia, in a changing climate during the 21st century, *Hydrological Research Letters*, **4**, 50–54.

Ninomiya, K., and T. Akiyama, 1992: Multi-scale features of Baiu, the summer monsoon over Japan and the East Asia. *J. Meteor. Soc. Japan*, **70**, 467–495.

Onogi, K., J. Tsutsui, H. Koide, M. Sakamoto, S. Kobayashi, H. Hatsushika, T. Matsumoto, N. Yamazaki, H. Kamahori, K. Takahashi, S. Kadokura, K. Wada, K. Kato, R. Oyama, T. Ose, N. Mannoji, and R. Taira, 2007: The JRA-25 reanalysis. *J. Meteor. Soc. Japan*, **85**, 369–432, doi:10.2151/jmsj.85.369.

Oouchi, K., J. Yoshimura, H. Yoshimura, R. Mizuta, S. Kusunoki, and A. Noda, 2006: Tropical cyclone climatology in a global-warming climate as simulated in a 20 km-mesh global atmospheric model: Frequency and wind intensity analyses. *J. Meteor. Soc. Japan*, **84**, 259–276, doi:10.2151/jmsj.84.259.

Rahman, Md. M., N. Ferdousi, Y. Sato, S. Kusunoki, and A. Kitoh, 2012: Rainfall and temperature scenario for Bangladesh using 20 km mesh AGCM. *Int. J. Climate Change Strategies and Management*, in press.

Rajendran, K., and A. Kitoh, 2008: Indian summer monsoon in future climate projection by a super-high-resolution global model. *Current Science*, **95**, 1560–1569.

Rajendran, K., A. Kitoh, R. Mizuta, S. Sajani, and T. Nakazawa, 2008: High resolution simulation of mean convection and its intraseasonal variability over the tropics in MRI/JMA 20-km Mesh AGCM. *J. Climate*, **21**, 3722–3739, doi: 10.1175/2008JCLI1950.1.

Randall, D., and D.-M. Pan, 1993: Implementation of the Arakawa-Schubert cumulus parameterization with a prognostic closure. *Meteorological Monograph/The representation of cumulus convection in numerical models*, **46**, 145–150.

Rayner, N. A., D. E. Parker, E. B. Horton, C. K. Folland, L. V. Alexander, D. P. Rowell, E. C. Kent, and A. Kaplan, 2003: Global analyses of sea surface temperature, sea ice, and night marine air temperature since the late nineteenth century. *J. Geophys. Res.*, **108(D14)**, 4407, doi:10.1029/2002JD002670.

Satoh, M., T. Matsuno, H. Tomita, H. Miura, T. Nasuno, and S. Iga, 2008: Nonhydrostatic Icosahedral Atmospheric Model (NICAM) for global cloud resolving simulations. *J. Computational Phys.*, **227**, 3486–3514, doi:10.1016/j.jcp.2007.02.006.

Shibata, K., and T. Aoki, 1989: An infrared radiative scheme for the numerical models of weather and climate. *J. Geophys. Res.*, **94**, 14923–14943.

Shibata, K., M. Deushi, T. T. Sekiyama, and H. Yoshimura, 2005: Development of an MRI chemical transport model for the study of stratospheric chemistry. *Pap. Meteor. Geophys.*, **55**, 75–118.

Shibata, K., and A. Uchiyama, 1992: Accuracy of the delta-four-stream approximation in inhomogeneous scattering atmospheres. *J. Meteor. Soc. Japan*, **70**, 1097–1109.

Smith, R. N. B., 1990: A scheme for predicting layer clouds and their water content in a general circulation model. *Quart. J. Roy. Meteor. Soc.*, **116**, 435–460, doi:10.1002/qj.49711649210.

Tanaka, T. Y., K. Orito, T. Sekiyama, K. Shibata, M. Chiba, and H. Tanaka, 2003: MASINGAR, a global tropospheric aerosol chemical transport model coupled with MRI/JMA98 GCM: Model description. *Pap. Meteor. Geophys.*, **53**, 119–138.

Taylor, K. E., 2001: Summarizing multiple aspects of model performance in a single diagram. *J. Geophys. Res.*, **106**, 7183–7192, doi:10.1029/2000JD900719.

Tiedtke, M., 1989: A comprehensive mass flux scheme for cumulus parameterization in large-scale models. *Mon. Wea. Rev.*, **117**, 1779–1800.

Tiedtke, M., 1993: Representation of clouds in large-scale models. *Mon. Wea. Rev.*, **121**, 3040–3061.

Unisys, 2011: Unisys weather hurricane tropical data. [Available online at http://weather.unisys.com/hurricane/].

Uppala, S. M., P. W. Kallberg, A. J. Simmons, U. Andrae, V. D. C. Bechtold, M. Fiorino, J. K. Gibson, J. Haseler, A. Hernandez, G. A. Kelly, X. Li, K. Onogi, S. Saarinen, N. Sokka, R. P. Allan, E. Andersson, K. Arpe, M. A. Balmaseda, A. C. M. Beljaars, L. Van De Berg, J. Bidlot, N. Bormann, S. Caires, F. Chevallier, A. Dethof, M. Dragosavac, M. Fisher, M. Fuentes, S. Hagemann, E. Holm, B. J. Hoskins, L. Isaksen, P. A. E. M. Janssen, R. Jenne, A. P. Mcnally, J.-F. Mahfouf, J.-J. Morcrette, N. A. Rayner, R. W. Saunders, P. Simon, A. Sterl, K. E. Trenberth, A. Untch, D. Vasiljevic, P. Viterbo, and J. Woollen, 2005: The ERA-40 reanalysis. *Quart. J. Roy. Meteor. Soc.*, **131**, 2961–3012.

Vergara, W., and S. M. Scholz, 2010: *Assessment of the risk of Amazon dieback: main report*. Environmentally and Socially Sustainable Development Department, The World Bank, 86 pp.

Wakazuki, Y., S. Kanada, C. Muroi, A. Hashimoto, T. Kato, M. Nakamura, A. Noda, M. Yoshizaki, and K. Yasunaga, 2007: Regional climate projection experiments on the Baiu frontal activity around the Japan islands using a non-hydrostatic cloud-system-resolving model. *J. Earth Simulator*, **8**, 13–25.

Waliser, D. E., K. Jin, I.-S. Kang, W. F. Stern, S. D. Schubert, M. L. C. Wu, K.-M. Lau, M.-I. Lee, V. Krishnamurthy, A. Kitoh, G. A. Meehl, V. Y. Galin, V. Satyan, S. K. Mandke, G. Wu, Y. Liu, and C.-K. Park, 2003: AGCM simulations of intraseasonal variability associated with the Asian summer monsoon. *Clim. Dyn.*, **21**, 423–446.

Wang, B., and H. Rui, 1990: Synoptic climatology of transient tropical intraseasonal convection anomalies 1975–1985. *Meteor. Atmos. Phys.*, **44**, 43–61.

Wang, B., R. Wu, and K. M. Lau, 2001: Interannual variability of the Asian summer monsoon: Contrasts between the Indian and the western North Pacific-East Asian monsoons. *J. Climate*, **14**, 4073–4090.

Wang, B., I.-S. Kang, and J.-Y. Lee, 2004: Ensemble simulations of Asian-Australian monsoon variability by 11 AGCMs. *J. Climate*, **17**, 803–818.

Webster, P. J., and S. Yang, 1992: Monsoon and ENSO: Selectively interactive systems. *Quart. J. Roy. Meteor. Soc.*, **118**, 877–926, doi:10.1002/qj.49711850705.

Xie, P., and P. A. Arkin, 1997: Global precipitation: a 17-year monthly analysis based on gauge observations, satellite estimates, and numerical model outputs. *Bull. Amer. Meteor. Soc.*, **78**, 2539–2558.

Xue, Y., F. Sales, W. K. M. Lau, A. Boone, J. Feng, P. Dirmeyer, Z. Guo, K.-M. Kim, A. Kitoh, V. Kumar, I. Poccard-Leclercq, N. Mahowald, W. Mufouma-Okia, P. Pegion, D. P. Rowell, J. Schemm, S. D. Schubert, A. Sealy, W. M. Thiaw, A. Vintzileos, S. F. Williams, and M.-L. C. Wu, 2010: Intercomparison and analyses of the climatology of the West African Monsoon in the West African Monsoon Modeling and Evaluation project (WAMME) first model intercomparison experiment. *Clim. Dyn.*, **35**, 3–27.

Yasunaga, K., M. Fujita, T. Ushiyama, K. Yoneyama, Y. N. Takayabu, and M. Yoshizaki, 2008: Diurnal variations in precipitable water observed by ship-borne GPS over the tropical Indian Ocean. *SOLA*, **4**, 97–100, doi:10.2151/sola.2008-025.

Yatagai, A., P. Xie, and A. Kitoh, 2005: Utilization of a new gauge-based daily precipitation dataset over monsoon Asia for validation of the daily precipitation climatology simulated by the MRI/JMA 20-km-mesh AGCM. *SOLA*, **1**, 193–196, doi:10.2151/sola.2005-050.

Yatagai, A., O. Arakawa, K. Kamiguchi, H. Kawamoto, M. Nodzu, and A. Hamada, 2009: A 44-year daily gridded precipitation dataset for Asia based on a dense network of rain gauges. *SOLA*, **5**, 137–140, doi:10.2151/sola.2009-035.

Yoshimura, H., and T. Matsumura, 2005: A two-time-level vertically-conservative semi-Lagrangian semi-implicit double Fourier series AGCM. *CAS/JSC WGNE Research Activities in Atmospheric and Ocean Modeling*, **35**, 3.27-3.28.

Yukimoto, S, H. Yoshimura, M. Hosaka, T. Sakami, H. Tsujino, M. Hirabara, T. Y. Tanaka, M. Deushi, A. Obata, H. Nakano, Y. Adachi, E. Shindo, S. Yabu, T. Ose and A. Kitoh, 2011: Meteorological Research Institute-Earth System Model v1 (MRI-ESM1)—Model description—. *Tech. Rep. Meteor. Res. Inst.*, **64**, 88 pp.

Zhao, M., I. M. Held, S.-J. Lin, and G. A. Vecchi, 2009: Simulations of global hurricane climatology, interannual variability, and response to global warming using a 50 km resolution GCM. *J. Climate*, **22**, 6653–6678, doi:10.1175/2009JCLI3049.1.